Energy dependent potentials determined by inversion: The $p+\alpha$ potential up to 65 MeV

S. G. Cooper and R. S. Mackintosh
Physics Department, The Open University, Milton Keynes, MK7 6AA, United Kingdom
(Received 13 February 1996)

The iterative perturbative inversion method is extended to determine explicitly energy and parity dependent potentials from S matrices specified at a series of discrete energies. The energy dependence is inserted only in the potential magnitude, although enhanced ''energy bite'' techniques allow this approximation to be tested. With a linear energy dependence in both real and imaginary components, S-matrix data for $p+\alpha$ scattering is fitted with a single potential for a wide range of energies above the inelastic threshold. The imaginary potential is shown to be parity dependent. The real potential is consistent, in both the potential shape and the parity and energy dependence, with potentials established for subthreshold energies. The method is also applied to resonating group model (RGM) phase shifts for $n+{}^{16}$O and $p+\alpha$ scattering to give energy and parity dependent potentials in both cases. For $p+\alpha$, a close correspondence is obtained between the RGM and the empirical potentials in both the energy and parity dependence up to about 65 MeV. For $n+{}^{16}$O, potentials are determined for positive and negative energies. [S0556-2813(96)03312-2]

PACS number(s): 25.40.Cm, 25.10+s, 24.10.Ht, 03.65.Nk

I. INTRODUCTION

Fixed energy S-matrix to potential inversion has now been used to establish local potentials for a wide range of scattering cases. However, most of the available methods (see Refs. [1–5]), will not handle spin-1/2 cases and are inappropriate to few-nucleon systems at low energies where very few partial waves contribute. Inversion is possible for such cases with the iterative perturbative (IP) inversion method. This can handle channel spin 1/2 and, by means of the ''mixed case'' extension [6,7] of fixed energy inversion,[1] can give meaningful results in cases where there is information from only a few partial waves. IP inversion also makes possible (i) the determination of parity dependent potentials, essential for few-nucleon cases, and (ii) the fitting of bound and resonant state energies. Point (ii) allows the determination of potentials which are valid over a range of both negative and positive energies [8]. Using these techniques, potentials have been determined from empirical phase shifts for $p+\alpha$ [6] and ^{3}He + α [8] scattering and from resonating group model (RGM) phase shifts for several low energy nucleon-nucleus cases, [9,10]. In most cases, parity dependent potentials are required to reproduce the phase shifts. These potentials have been applied in reaction studies, for example, the three-body model for ^{6}He [11] or (α,γ) capture reactions [12].

One problem, not properly addressed up to now, is that many local potentials are energy dependent. The nucleon-nucleus potential is an obvious example [9,10]. Energy dependence has been established by applying inversion at a sequence of energies [6]. However, it is useful to have energy dependent potentials that can be evaluated at any required energy, and having energy dependence parameters that can be directly compared with those of theoretical or empirical models. Not only are such potentials required for many applications, but inversion may sometimes be impossible without energy dependence. For example, mixed case inversion for energies just above the inelastic threshold is only possible when energy dependence is explicitly included in the imaginary components. Empirical S matrices which have been established for $p+\alpha$ scattering in several phase shift analyses above the inelastic threshold [13–16] are inaccessible both to energy independent inversion and to the energy bite techniques previously used to establish energy dependence.

Our first aim in this paper is to present and test a substantial new extension of the IP method to energy dependent inversion. For any S-matrix elements given at discrete energies E_i or parametrized over a range of energies, inversion is applied to determine the energy dependent potential that reproduces the given S matrix. Symbolically,

$$S_{lj}(E_i) \quad \text{or} \quad S_{lj}(E) \rightarrow V(E,r)+\mathbf{l}\cdot\boldsymbol{\sigma}V_{\mathrm{so}}(E,r).$$

Bound state and resonance energies can be fitted at the same time, leading to a consistent representation of bound and scattering states. The energy dependence of each potential component (i.e., real, imaginary, parity dependent or parity independent, central or spin orbit) is treated separately. The major restriction at present is that the radial geometry of all components of the potential is held fixed; previous mixed case studies for $p+\alpha$ suggested that this approximation is reasonable. It is straightforward to avoid ambiguities arising from supersymmetry [17].

The first application is to theoretical (RGM) phase shifts for $p+\alpha$ and $n+{}^{16}$O scattering, for energies up to 50 MeV and 30 MeV (c.m.), respectively [18,19]. The smooth energy dependence of the RGM phase shifts permits very precise inversions and should provide an ideal test. Previous ''energy bite'' analyses revealed that both the parity dependent and parity independent components of the potential were strongly energy dependent, but the bound states energies for $n+{}^{16}$O were not reproduced. Applying energy dependent in-

[1] ''Mixed case'' inversion is intermediate between fixed energy inversion and fixed partial wave inversion; i.e., one determines a potential from $S_{lj}(E_i)$ for a limited set of lj and energies E_i.

version over energy bites allows us to assess the energy dependence of the potential geometry.

The second major objective here is to present potentials obtained by inversion of S matrices at energies above the inelastic threshold. Three sets of empirical data are considered [13–15] extending to 70 MeV. Allowing for parity dependence, corresponding degrees of freedom are necessary. However, only four extra parameters are required, additional to those necessary for energy independent inversion, so that energy dependent inversion yields an extremely economical description of considerable data.

In order to study the continuity (or otherwise) of the real parts at the inelastic threshold and to compare the energy dependent empirical potentials with the RGM potentials, energy dependent inversion is also applied to the subthreshold phase shifts previously studied [6]. A more complete comparison than previously made is now possible [9,10] between the real empirical and RGM-derived potentials over a wide energy range, establishing the contributions of antisymmetrization to the radial shape, depth, and energy dependence of the empirical potential.

Parity dependence in the imaginary components of the empirical potential can now be studied. Some contribution is expected due to the effect of the underlying nonlocality which couples the imaginary potential with the strong parity dependence in the real components. Evidence for this effect is found in the empirical S matrices, for which $|S|$ is markedly <1 for $l=2$. Fixed energy inversion at 65 MeV also gives smoother potentials if the parity dependence is permitted in both real and imaginary components [10].

Energy dependence has been included in conventional optical model fits to subthreshold $p+\alpha$ scattering data; see, e.g., [20]. Energy dependence was introduced into the real potential either as a linear energy dependence of the depth or in the Woods-Saxon radius parameter. However, with the limitations of the optical potential geometry, the imperfect reproduction of the data and absence of parity dependence imply that such fits provide no conclusive evidence concerning the $p+\alpha$ energy dependence.

The structure of the paper is as follows. The IP procedure is reviewed in the first part of Sec. II. A method for determining energy dependent potentials is then presented in the second part of Sec. II. In Sec. III, energy dependent potentials are determined from RGM phase shifts for both $p+\alpha$ and $n+{}^{16}\mathrm{O}$. In Sec. IV the procedure is applied to empirical phase shifts for $p+\alpha$ scattering, first below and second above the inelastic threshold. In Sec. V the results of the various inversions for $p+\alpha$ are compared to ascertain the general features of the $p+\alpha$ potential which have been established for the complete energy range up to ~ 65 MeV. The comparison with the results of the inversions from the RGM phase shifts is used to establish which features in the resultant potential can be reliably ascribed as due to the affects of antisymmetrisation. Finally conclusions are presented. In the following text we refer at several points to Ref. [21], in which fuller details and further discussion can be found.

II. GENERALIZING THE IP INVERSION PROCEDURE

A. IP procedure and parity dependence

The iterative-perturbative (IP) procedure was first developed for fixed energy spin-0 scattering [22] and extended to spin 1/2 [23]. The method has been further extended to mixed-case inversion [7], which also permits the application of ''energy bite'' techniques for inversion of phase shifts parametrized as a function of energy [6]. An additional adaptation allows inversion from both bound and resonant state energies [8]. Although the iterative-perturbative inversion method has been described in many previous publications, for example [24], the essentials of the method, together with some of these extensions, are repeated here to define certain terms frequently referred to later. The considerable versatility of the procedure allows further extensions to be incorporated, such as the determination of parity dependent potentials in a single inversion and the inclusion of s-wave scattering length as input data. Previously, parity dependent potentials were established by separate inversions on even or odd partial waves, but it is more convenient to determine both the parity independent and parity dependent components simultaneously when energy dependence is also included. All the features of the IP procedure described below are embodied in the code IMAGO [25] which we can make available.

In general, the input or ''target'' data for the inversion consists of real or complex elastic scattering phase shifts for one or more energies. They may also include a set of known bound and resonant state energies and the s-wave scattering length. The procedure outlined below applies for both spin-0 and spin-1/2 scattering. The resulting potential may be either real or complex and, where appropriate, have spin-orbit and parity dependent components.

In the following discussion, the partial wave index κ defines both the quantum numbers l,j and the energy E, corresponding to the wave number k (unless stated otherwise all energies quoted are laboratory energies). A complex S-matrix element for given κ in the target set is denoted S_κ^{tar} and N_κ represents the total number of complex phase shifts. The index n denotes a specific bound (or resonant) state which, in addition to the l,j and state energy E_n, also defines the number of radial nodes in the state wave function. Then N_n denotes the total number of bound or resonant states.

The potential resulting from the inversion should be a close approximation to the potential $V^{\mathrm{tar}}(r)$, which satisfies the radial Schrödinger equation

$$\left[-\frac{d^2}{dr^2}+\frac{l(l+1)}{r^2}+\frac{2\mu}{\hbar^2}[V_{\mathrm{C}}(r)+V^{\mathrm{tar}}(r)]-k^2\right]u_\kappa(r)=0, \tag{1}$$

for all values of κ. $V_{\mathrm{C}}(r)$ is a standard Coulomb potential and the constants use conventional definitions. Asymptotically, the radial wave function $u_\kappa(r)$ satisfies

$$u_\kappa(r)\simeq I_\kappa(r)-S_\kappa^{\mathrm{tar}}O_\kappa(r), \tag{2}$$

where I_κ and O_κ are the ingoing and outgoing Coulomb wave functions, respectively, for given l and E. If the target data include bound or resonant states, $V^{\mathrm{tar}}(r)$ must also satisfy the bound state radial Schrödinger equation for each n. The resultant real wave function $\phi^n(r)$ then behaves asymptotically as $\phi^n(r)\sim O_l^-(r)$ or $\phi^n(r)\sim G_l(r)$ for bound or resonant states, respectively.

In practice the potential calculated by inversion, $V^{\rm inv}(r)$, will not be identical to $V^{\rm tar}(r)$, for example, because of irregularities in the target data which should not be fitted. It is convenient to define a quantity σ^2 which measures how closely the target data set is reproduced by $V^{\rm inv}(r)$. This measure contains separate contributions from the S-matrix elements and from the bound or resonant states. Replacing $V^{\rm tar}(r)$ and $S_\kappa^{\rm tar}$ in Eqs. (1) and (2) with $V^{\rm inv}(r)$ and $S_\kappa^{\rm inv}$, respectively, defines the S matrix $\mathbf{S}^{\rm inv}$, which in general $\neq \mathbf{S}^{\rm tar}$. For the bound or resonant states, two solutions ϕ_1^n and ϕ_2^n, corresponding to the regions inside and outside the matching radius $r=R_{\rm m}$, respectively, are calculated using the Schrödinger equation with the potential $V^{\rm inv}(r)$ and target energy E_n. The function ϕ_1^n is calculated by integrating the Schrödinger equation outwards from the origin and must contain the correct number of radial nodes. The function ϕ_2^n is determined by integrating inwards from the correct asymptotic form at large radii. A valid solution is obtained only if the logarithmic derivatives of ϕ_1^n and ϕ_2^n, respectively, $r\phi'^n_1/\phi_1^n$ and $r\phi'^n_2/\phi_2^n$, are equal at $r=R_{\rm m}$. In general this is not true and there are two alternative procedures which may now be used. An energy $E_n^{\rm inv}$ may be inserted into the Schrödinger equation, in place of E_n, and varied until the wave functions obtained for the two regions match correctly at $r=R_{\rm m}$. However, it is more convenient here to work with the logarithmic derivatives. Finally, the phase shift distance σ^2 is defined as

$$\sigma^2=\sum_\kappa w_\kappa^2|S_\kappa^{\rm tar}-S_\kappa^{\rm inv}|^2+W^2\sum_n \left|\frac{\phi'^n_2}{\phi_2^n}-\frac{\phi'^n_1}{\phi_1^n}\right|^2_{r=R_{\rm m}}. \quad (3)$$

The term w_κ represents a weighting factor, which by default is unity for all κ, but may be varied either to give more emphasis on the higher l or to incorporate the estimated errors in the empirical S matrix (see Ref. [24] for further details). The second weighting factor W establishes the relative accuracy to which $V^{\rm inv}(r)$ determines the bound state energies compared to the accuracy to which $V^{\rm inv}(r)$ determines $\mathbf{S}^{\rm tar}$.

At the start of the procedure an initial choice of $V^{\rm inv}(r)$ is required, i.e., the ''starting reference potential,'' denoted $V^{\rm srp}(r)$. Up to eight components may be required for $V^{\rm inv}(r)$. Above the inelastic threshold $V^{\rm inv}(r)$ must be complex. For spin-1/2 scattering both central, $V_{\rm cen}(r)+iW_{\rm cen}(r)$ and spin-orbit terms $2\mathbf{l}\cdot\mathbf{s}[V_{\rm so}(r)+iW_{\rm so}(r)]$ are required, and where parity dependence is necessary, each of $V_{\rm cen}(r)$, $W_{\rm cen}(r)$, $V_{\rm so}(r)$, or $W_{\rm so}(r)$ can have the form $V_1(r)+(-1)^lV_2(r)$. Each of the possible eight components is treated independently in the inversion. The subscript c refers to a particular component. Some or all of the eight possible components may be zero in the starting reference potential.

To minimize σ^2, perturbations must be added to $V^{\rm inv}(r)$ or, initially, $V^{\rm srp}(r)$. These perturbations are added separately to each potential component and are obtained from an expansion over N_c^b basis functions $v_{ci}(r)$. The resulting potential is obtained:

$$V_c^{\rm new}(r)=V_c^{\rm inv}(r)+\sum_{i=1}^{N_c^b}\lambda_{ci}v_{ci}(r), \quad (4)$$

where the λ_{ci} are expansion coefficients to be optimized by the inversion. Typically Gaussian or zeroth order Bessel functions are used for the $v_{ci}(r)$, although the functions should be linearly independent.

For a small potential perturbation $\lambda_{ci}v_{ci}(r)$, the Born approximation can be applied to obtain an approximate expression for the related change in the S-matrix element $\delta S_\kappa=S_\kappa^{\rm new}-S_\kappa^{\rm inv}$, i.e.,

$$\delta S_\kappa=\left(-\frac{i\lambda_{ci}\mu C_c}{\hbar^2k_\kappa}\right)\int_0^\infty v_{ci}(r)[u_\kappa(r)]^2dr, \quad (5)$$

where $u_\kappa(r)$ is the radial wave function obtained from the Schrödinger equation for the index κ using the potential $V^{\rm inv}(r)$. The coefficient C_c is a constant specific to the potential component c. For the real and imaginary terms C_c is set equal to 1 and i, respectively. For the spin-orbit terms C_c is further multiplied by $2\langle\mathbf{l}\cdot\mathbf{s}\rangle$ and for the parity dependent terms V_2, C_c is additionally multiplied by $(-1)^l$. A term corresponding to the imaginary spin-orbit parity dependent potential then has $C_c=2\,i\langle\mathbf{l}\cdot\mathbf{s}\rangle(-1)^l$.

In the case of bound or resonant states, the perturbation is added to $V^{\rm inv}(r)$ to correct the difference between the logarithmic derivatives of ϕ_1^n and ϕ_2^n at $r=R_{\rm m}$. As above, the Born approximation can be applied to a small change in the real potential, $\lambda_{ci}v_{ci}(r)$, to obtain a simple expression for λ_{ci}, i.e.,

$$\lambda_{ci}C_c\left\{\frac{1}{[\phi_1^n(R)]^2}\int_0^R v_{ci}(r)[\phi_1^n(r)]^2dr+\frac{1}{[\phi_2^n(R)]^2}\int_R^{R_{\rm m}} v_{ci}(r)[\phi_2^n(r)]^2dr\right\}=\left(\frac{\phi'^n_2}{\phi_2^n}-\frac{\phi_1'^n}{\phi_1^n}\right)_{r=R_{\rm m}}. \quad (6)$$

Equations (5) and (6) define a set of first derivatives of either $S_\kappa^{\rm inv}$ or $\phi'^n_1/\phi_1^n-\phi'^n_2/\phi_2^n$ which are linearly dependent on λ_{ci}. These equations can now be inserted into the least squares minimization of σ^2. A set of linear equations is then obtained which are overdetermined if $(\Sigma_cN_c^b)<N_n+2N_\kappa$. The solutions for the λ_{ci} are obtained by applying singular value decomposition (SVD) to solve the matrix equations. This process permits the introduction of a tolerance limit to eliminate the smallest singular values, so that for any reasonable basis and starting reference potential an optimized set of expansion coefficients λ_{ci} can be calculated. These λ_{ci} determine a new potential $V^{\rm new}(r)$, for which the corresponding value of σ^2 should be smaller than that for $V^{\rm srp}(r)$.

The above process can be repeated on an iterative basis, until satisfactory convergence is achieved. While the introduction of parity dependence introduces some ambiguities into the inversion, notably near the origin, the problem is ameliorated by imposing a restriction to smooth potentials by use of a truncated basis and a high SVD tolerance.

Using expressions closely analogous to those above, the IP procedure can also be extended to fit the scattering length at zero energy [21].

B. Determining energy dependent potentials

The IP procedure is easily extended to determine energy dependent potentials, under the assumption that the potential geometry is independent of energy. The method is sufficiently versatile to permit the introduction of further modifications to overcome the restriction if necessary. In subsequent sections an extension of the energy bite technique [6] is introduced which permits a more detailed investigation of the energy dependence of the potential shape. The complete procedure has been implemented in the code IMAGO [25].

If the geometry is independent of energy, any potential component c can be expressed in the form

$$V_c(E,r)=F_c(E)U_c(r),$$

with $F_c(E)$ defined separately for each component. Components can then be kept energy independent in the inversion, if appropriate. Separate functions are required for the real and imaginary potentials.

For the real components, the most general form of the energy dependence $F_c(E)$ is obtained from an expansion over a set of N_c^E energy dependent basis functions $f_{ci}(E-E_{\rm ref})$ analogous to the radial basis functions $V_i(r)$ [now added only to $U_c(r)$], i.e.,

$$F_c(E)=1+\sum_i^{N_c^E}\xi_{ci}f_{ci}(E-E_{\rm ref}), \tag{7}$$

where $E_{\rm ref}$ is a fixed reference energy and the ξ_{ci} are energy expansion coefficients determined in the inversion. The function $U_c(r)$ then specifies the potential component c at $E=E_{\rm ref}$. The simplest form of energy dependence is the linear form $F_c(E)=1+\xi_cE$, sufficient in many practical cases. The applications of the procedure in Secs. III and IV additionally use the functions $f_{ci}(E)=E^i$ and $f_{ci}(E)=E^{1/i}$.

For the imaginary components, a slightly different expression for the energy dependence is required to ensure that the potentials vanish at the inelastic threshold, $E=E_0$. In the following formulation it is implicitly assumed that the imaginary components are zero below the inelastic threshold, i.e., for $E<E_0$, $F_c(E)=0$. A further reference energy, $E'_{\rm ref}>E_0$, is required. The most general form considered here is

$$F_c(E)=\left(\frac{E-E_0}{E'_{\rm ref}-E_0}\right)^p+\sum_i^{N_c^{\rm E}}\xi_{ci}g_{ci}(E-E_{\rm ref}). \tag{8}$$

Here p is chosen to optimize the inversion and the functions $g_{ci}(E)$ must satisfy $g_{ci}(E)\to 0$ as $E\to E_0$. The $g_{ci}(E)$ consequently differ from the functions $f_{ci}(E)$ used in Eq. (7). For a linear energy dependence $p=1$ and no further expansion coefficient is required because the energy gradient is jointly determined by $E'_{\rm ref}$ and the magnitude of $U_c(r)$.

The energy dependent potential $V_c^{\rm inv}(E,r)=F_c^{\rm inv}(E)U_c^{\rm inv}(r)$ is expanded:

$$V_c^{\rm new}(r,E)=\left[F_c^{\rm inv}(E)+\sum_{i=1}^{N_c^E}\xi_{ci}f_{ci}(E-E_{\rm ref})\right]\times\left[U_c^{\rm inv}(r)+\sum_{i=1}^{N_c^b}\lambda_{ci}v_{ci}(r)\right], \tag{9}$$

with an equivalent form for the imaginary components. To first order, the cross terms $f_{ci}(E-E_{\rm ref})v_{ci}(r)$ can be neglected, leaving the perturbation

$$U_c^{\rm inv}(r)\sum_{i=1}^{N_c^E}\xi_{ci}f_{ci}(E-E_{\rm ref})+F_c^{\rm inv}(E)\sum_{i=1}^{N_c^b}\lambda_{ci}v_{ci}(r), \tag{10}$$

which is linear in both f_{ci} and $v_{ci}(r)$. For a small perturbation $F_c^{\rm inv}(E)\lambda_{ci}v_{ci}(r)$, the Born approximation yields a correction for $\delta S_\kappa=S_\kappa^{\rm new}-S_\kappa^{\rm inv}$ which is identical to Eq. (5) except that the right hand side of the equation must be multiplied by the additional factor $F_c^{\rm inv}(E_\kappa)$. The correction to S_κ arising from a small perturbation in the energy dependence, $U_c^{\rm inv}(r)\xi_{ci}f_{ci}(E-E_{\rm ref})$, is similar, giving

$$\delta S_\kappa=\left(-\frac{i\xi_{ci}\mu C_c f_{ci}(E_\kappa-E_{\rm ref})}{\hbar^2k_\kappa}\right)\int_0^\infty U_c^{\rm inv}(r)[u_\kappa(r)]^2dr, \tag{11}$$

where all other coefficients are as defined previously. Equivalent terms can be obtained for the imaginary perturbations.

In the case of the bound or resonant states, the correction to the logarithmic derivatives follow from Eq. (6). The corrections for $F_c^{\rm inv}(E_n^{\rm inv})\lambda_{ci}v_{ci}(r)$ are obtained by multiplying the left hand side of Eq. (6) by $F_c^{\rm inv}(E_n^{\rm inv})$. For the perturbation $U_c^{\rm inv}(r)\xi_{ci}f_{ci}(E_n^{\rm inv}-E_{\rm ref})$ the correction becomes

$$\xi_{ci}f_{ci}(E_n^{\rm inv}-E_{\rm ref})C_c\left\{\frac{1}{[\phi_1^n(R)]^2}\int_0^R U_c^{\rm inv}(r)[\phi_1^n(r)]^2dr+\frac{1}{[\phi_2^n(R)]^2}\int_R^{R_{\rm m}}U_c^{\rm inv}(r)[\phi_2^n(r)]^2dr\right\}=\left(\frac{\phi_2'^n}{\phi_2^n}-\frac{\phi_1'^n}{\phi_1^n}\right)_{r=R_{\rm m}}. \tag{12}$$

Equations (11) and (12) define changes in the S-matrix elements or the logarithmic derivatives of ϕ_1^n and ϕ_2^n which are approximately linear in both ξ_{ci} and λ_{ci}. A least squares minimization of σ^2, following the procedure in Sec. II A, then produces a set of linear equations for ξ_{ci} and λ_{ci} and SVD techniques can be applied, as before, to determine the unknown coefficients. The equations remain overdetermined providing that

$$\sum_c (N_c^b+N_c^E)<N_n+2N_\kappa.$$

The relative importance of the two sets of functions can be introduced by varying the magnitude of one set of basis functions.

III. ENERGY DEPENDENT POTENTIALS FROM RGM PHASE SHIFTS

Phase shifts from theoretical models such as the single-channel RGM provide an ideal test case for the new inversion techniques since the phase shifts, having no experimental ''noise,'' should be very precisely reproduced. Energy dependent real potentials are here determined by inversion of RGM phase shifts for $p+\alpha$ and $n+{}^{16}$O scattering. The data for the latter case include two bound state energies.

In a previous study [9] of $p+\alpha$ at energies below the inelastic threshold, inversion of the RGM phase shifts yielded parity dependent potentials very similar to those determined from empirical data. The restriction to the single-channel RGM did not greatly effect the energy dependence of these potentials. The parity dependent potentials for both $p+\alpha$ and $n+{}^{16}$O scattering have also been investigated over a much wider energy range, as part of an extensive study of the nucleon + nucleus potential in which fixed energy inversion using narrow energy bites was applied to single channel RGM phase shifts [10]. For both target nuclei, the central parity independent (V_1) components varied approximately linearly with energy and the potential geometry had no clearly discernible dependence on energy. The central parity dependent (V_2) components were found to be very different for the two cases, but, in both cases, the magnitude decreased with energy. For the $p+\alpha$ case, the geometry of the V_2 term depended weakly on energy, although this dependence might have arisen due to the restriction to a small inversion basis. For $n+{}^{16}$O scattering, the V_2 term was much smaller but the geometry had a significant variation with energy, so that the new techniques may be less appropriate. The two bound states predicted by the RGM theory for the $n+{}^{16}$O case cannot be reproduced by energy independent potentials obtained by inversion from narrow energy bites.

A. $p+\alpha$ potential

1. Energy dependence of the potential geometry

The phase shifts of Reichstein and Tang [18] are here reanalyzed to assess how well simple forms of energy dependence can fit the phase shifts for a wide range of energies. However, before inverting the tabulated phase shifts for the entire energy range 0–50 MeV (c.m.), the energy dependence of the radial geometry is studied as follows: An effective range parametrization of the tabulated RGM phase shifts is evaluated over wide energy bites $E_{\rm cen}\pm 1$ MeV (c.m.). Energy dependent potentials with parity dependent, central, and spin-orbit components, of the form $U_c(r)(1+\xi_{c\,1}E)$ for each component, are then determined by inversion of these 2 MeV ''wide'' sequences of phase shifts for all l values. In this way, potentials are calculated for $E_{\rm cen}$ = 10, 20, 30, 40, and 50 MeV (c.m.), with $E_{\rm ref}=0$ in all cases.

In Fig. 1 potentials are presented for $E_{\rm cen}=10$, 30, and 50 MeV evaluated at $E=0$ [i.e., $U_c(r)$] and the expansion coefficients ξ_{ci} are tabulated in Table I for all cases. (The ξ_{ci} are given in terms of laboratory energies to allow a direct comparison in later sections with calculations from empirical phase shifts.) Comparing the new potentials with the previously determined energy independent potentials (shown in Fig. 2 of Ref. [10]) reveals that much of the energy dependence has been incorporated into the coefficients ξ_{ci}. The differences between the various $U_c(r)$ are remarkably small, particularly for the central V_1 component. In effect, potentials are determined for energies of 29–31 MeV and 49–51 MeV which, when extrapolated back to zero energy, are in remarkable agreement in both magnitude and radial shape. Some of the residual differences may be due to the increasing numbers of partial waves which contribute as $E_{\rm cen}$ in-

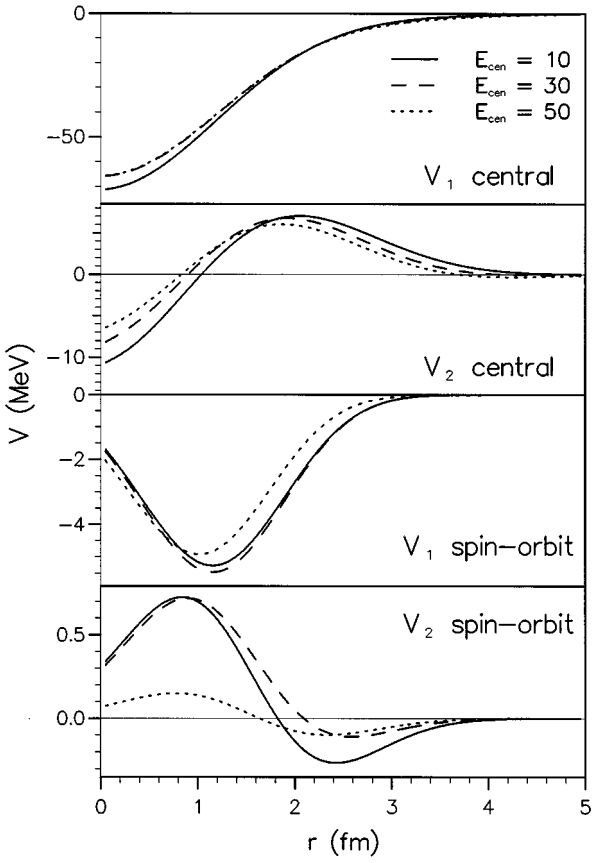

FIG. 1. For $p+\alpha$, the real zero energy radial potentials $U_c(r)$ for the central and spin-orbit V_1 and V_2 components obtained by inversion of RGM phase shifts over the energy bites $E_{\rm cen}\pm 1$ MeV centered at the energies $E_{\rm cen}=10$ MeV (solid lines), $E_{\rm cen}=30$ MeV (dashed lines), and $E_{\rm cen}=50$ MeV (dotted lines).

TABLE I. The coefficients $\xi_{c\,1}$ in MeV^{-1} for the four real potential components calculated from RGM phase shifts for the five energy bites $E_{\rm cen}\pm 1$ MeV.

$E_{\rm cen}$	Central V_1	Central V_2	Spin orbit V_1	Spin orbit V_2
10.0	−0.0049	−0.0180	0.0122	−0.00051
20.0	−0.0033	−0.0131	0.0128	−0.00040
30.0	−0.0036	−0.0130	0.0075	0.00002
40.0	−0.0036	−0.0117	0.0060	−0.000061
50.0	−0.0037	−0.0096	0.0151	−0.00269

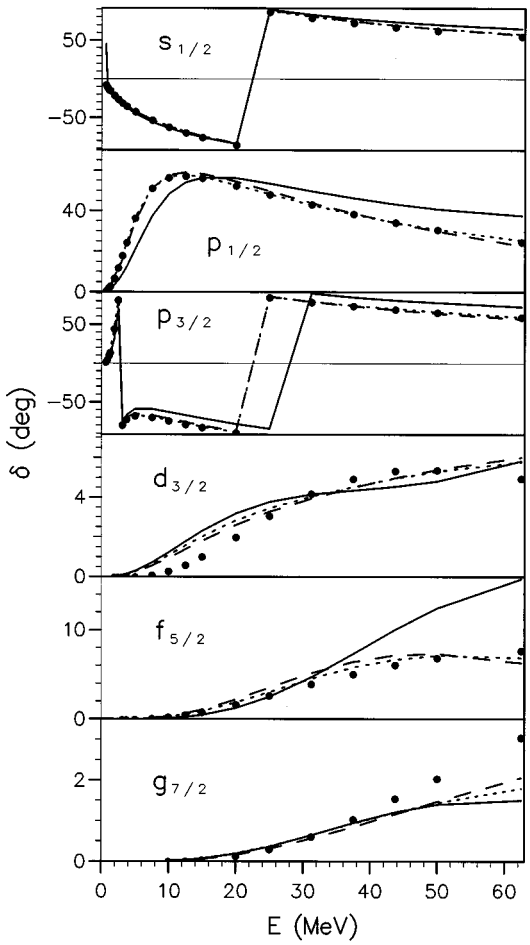

FIG. 2. For $p+\alpha$, RGM phase shifts (solid dots) for the partial waves $s_{1/2}$, $p_{1/2}$, $p_{3/2}$, $d_{3/2}$, $f_{5/2}$, and $g_{7/2}$ compared with the results of inversion using an energy independent potential, case (1) (solid lines), and two energy dependent potentials, solutions (2) (dashed lines) and (4) (dotted line), as described in the text.

creases. At $E_{\rm cen}=10$ MeV, the two lowest partial waves dominate the inversion more effectively than at the higher energies. Differences between the spin orbit components at $E_{\rm cen}=50$ MeV and at other energies are due to the influence of the h-wave phase shifts.

The volume integral of $U_c(r)$ for the central V_1 component increases from 532.8 to 578.2 MeV fm^3 as $E_{\rm cen}$ increases from 10 to 50 MeV (but corresponding to an overall decrease with energy in volume integral of the complete energy dependent potential). The corresponding rms radius of $U_c(r)$ increases from 2.32 to 2.55 fm. For the central V_2 component, the magnitude of the volume integral and the rms radius of $U_c(r)$ both decrease more dramatically with $E_{\rm cen}$, from 218.9 to 106.1 MeV fm^3 for the volume integral and from 2.83 to 1.32 for the rms radius for the same energy range. Overall, the energy dependence of the potential geometry is relatively small for the central V_1 term but is larger for the V_2 component. This energy dependence in V_2 will limit the accuracy to which the phase shifts from 0 to 50 MeV can be fitted with a fixed geometry potential.

The coefficients ξ_{ci} for both the V_1 and V_2 components reflect the expected decrease in the potential magnitude with increasing energy, with the central V_2 term having the strongest energy dependence. The energy dependence is not completely linear since the ξ_{ci} decrease in magnitude fairly systematically with $E_{\rm cen}$ for the central V_2 component. For the spin-orbit potential, the ξ_{ci} do not represent a consistent energy dependence, but the values of ξ_{ci} for the V_2 component are much smaller than for the other components. Nonlinear terms may be necessary in the inversion over a wider energy range.

2. Energy dependent potentials fitting 0 to 50 MeV (c.m.)

Potentials are presented below determined from (real) RGM phase shifts for the entire energy range from 0 to 50 MeV (c.m.). The following forms of the energy dependence $F_c(E)$ are considered.

(1) Energy independence $V_c(r)=U_c(r)$, $F_c(E)=1$.

(2) Linear energy dependence

$$V_c(E,r)=U_c(r)(1+\xi_{c\,1}E).$$

(3) Expansion in powers of E, i.e.,

$$V_c(E,r)=U_c(r)(1+\xi_{c\,1}E+\xi_{c\,2}E^2+\cdots).$$

(4) Energy expansion of the form

$$V_c(E,r)=U_c(r)(1+\xi_{c\,2}\sqrt{E}+\xi_{c\,1}E).$$

The inversion for these four cases gave σ = 2.07, 0.39, 0.30, and 0.20, respectively. The phase shifts cannot be reproduced precisely, since the potential geometry is fixed over this energy range, as discussed above. These are shown in Fig. 2 for cases (1), (2), and (4) together with the RGM phase shifts (shown as solid circles) for selected l,j values. In the corresponding comparisons for the $d_{5/2}$, $f_{7/2}$, $g_{9/2}$, and h partial waves, the RGM phase shifts are reproduced to an accuracy at least that of the $d_{3/2}$ and $g_{7/2}$ phase shifts. The energy independent potential (1) clearly gives an inadequate description of the RGM phase shifts and the introduction of just a linear energy dependence provides a significant improvement. Further relatively small improvements follow from the addition of higher order terms in the energy dependent expansion. The most successful expansion is case (4) containing the term $\sim\sqrt{E}$. Used alone, an energy expansion $\propto\sqrt{E}$ leads to a greater energy dependence at lower energies as is consistent with the coefficients, ξ_{ci} in Table I.

The radial functions $U_c(r)$ (potentials evaluated at $E=0$) are displayed in Fig. 3. There are significant differences between the energy independent and the energy dependent solutions for the central V_1 and the spin-orbit V_2 components. The different shape for case (1) probably compensates for the lack of energy dependence. The three energy dependent solutions agree more closely, particularly for the central V_1 term and, for this term, the potentials $V_c(E,r)$ are closest at $E\sim 25$ MeV, i.e., near the center of the energy range included in the inversion. However, the central V_2 and spin-orbit V_1 components are more consistent towards 50 MeV (c.m.), presumably because of the larger influence of the higher l values. This overall behavior is confirmed by examining the volume integrals [21]. The spin-orbit volume integrals show a considerable consistency which suggests that the apparent radial differences between

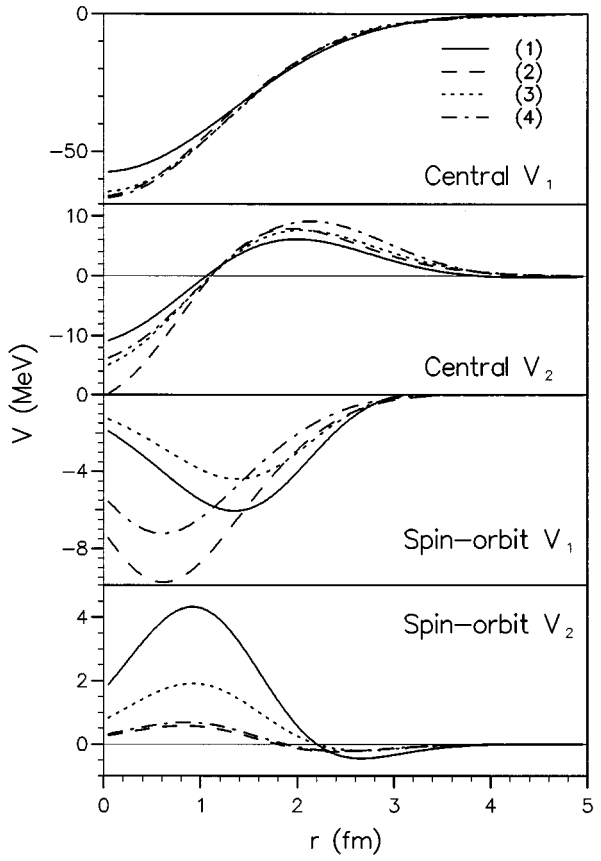

FIG. 3. For $p+\alpha$, the real zero energy potentials $U_c(r)$ determined by inversion from RGM phase shifts for the energy range up to 62.5 MeV (lab) corresponding to the four forms of energy dependence described in the text, (1) solid lines, (2) dashed line, (3) dotted lines, and (4) dash-dotted lines.

solutions (1) and (2) and solutions (3) and (4) simply reflect the limitations of inversion with energy independent radial forms.

The expansion coefficients ξ_{ci} for the energy dependent potentials are tabulated in Table II. For solutions (3) and (4) the coefficients are only listed to second order but, where a third term has been included, for all potential components $\xi_{c\,3}$ is very small. The coefficients for solution (3) represent only a small modification to the coefficients for the linear solution (2).

The small fall in σ due to the terms beyond second order suggests that a good representation of $F_c(E)$ has been obtained. Further reductions in σ require an energy dependent potential geometry and this is confirmed by inversions confined to a more restricted energy range [21].

3. Effects of channel coupling

The sensitivity of the potentials to the details of the RGM calculations has been investigated by using two alternative sets of RGM phase shifts [9], which, respectively, include and exclude coupling to the $d+{}^3$He channel. Potentials linearly dependent on energy, as in solution (2) in the preceding section, have also been determined for both the single-channel (SC) and coupled channel (CC) cases. The phase shifts are calculated only for energies below the inelastic threshold at 23 MeV (lab), but the resulting potentials reproduce the phase shifts accurately up to the threshold energy. The potentials determined in the SC calculation now differ slightly from the previously established solution (2) in that the central V_1 component is slightly deeper and the central V_2 component is reduced in magnitude. These differences reflect the different N-N interactions and other details of the RGM calculations. The coefficients $\xi_{c\,1}$ are -0.0061 and -0.0168 MeV^{-1} for the central V_1 and V_2 components, respectively. The corresponding potentials obtained from the CC phase shifts have very similar $U_c(r)$, although the coefficients $\xi_{c\,1}$ for the central V_1 and V_2 coefficients are -0.0066 and -0.0196 MeV^{-1}, respectively.

We conclude that general features of the energy dependent potential are not very dependent on the particular nucleon-nucleon potential used in the RGM calculation. The coupling to the $d+{}^3$He channel does not significantly affect the potential except to increase the energy dependence of the parity dependent term.

B. $n+{}^{16}$O potential

Energy dependent potentials for $n+{}^{16}$O are obtained by inversion of the single-channel RGM phase shifts [19] studied previously with fixed energy inversion [10]. The phase shifts are tabulated up to $E=30$ MeV (c.m.) and two bound states are predicted by the RGM, for $l=0$ at -3.26 MeV and $l=2$ at -1.50 MeV. The RGM calculations treat $n+{}^{16}$O as spin-0 scattering and only central but parity dependent potentials are determined.

Inversion of phase shifts for the complete energy range is not satisfactory, leading to a highly irregular radial shape for the V_2 component. This is probably due to the strongly energy dependent radial shape revealed by fixed energy studies. However, potentials which depend linearly on energy, and having a reasonable radial geometry, can be obtained by inversion over smaller energy ranges, up to 10 MeV wide.

TABLE II. The coefficients ξ_{ci} in MeV^{-1}, up to $i=2$, for the four components (labeled $c=1$–4) determined by inversion using three energy dependent expansions [the cases (2)–(4) described in the text] from RGM phase shifts for $E=0$ to 50 MeV (c.m.).

	Central V_1		Central V_2		Spin orbit V_1		Spin orbit V_2	
Case	ξ_{11}	ξ_{12}	ξ_{21}	ξ_{22}	ξ_{31}	ξ_{32}	ξ_{41}	ξ_{42}
(2)	-0.0038		-0.0137		0.0024		-0.0086	
(3)	-0.0038	-0.000007	-0.0138	-0.0002	0.0077	-0.00003	-0.0113	-0.0002
(4)	-0.0030	-0.0034	0.0013	-0.1151	-0.0069	0.1276	-0.0102	0.0053

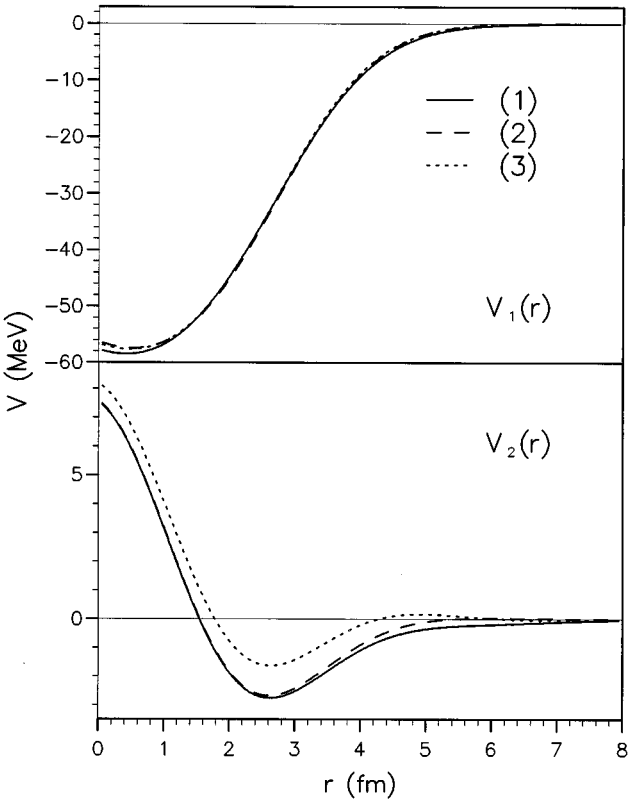

FIG. 4. For $p+{}^{16}$O, the real zero energy potentials $U_c(r)$ determined by inversion of RGM phase shifts and bound state energies. The inversions are made for three energy intervals, -5–5 MeV and including bound state energies (solid lines), 5–15 MeV (dashed lines), and 15–25 MeV (dotted lines), all as c.m. energies.

Three potentials have been determined from RGM phase shifts for the energy ranges: (1) -5–5 MeV, (2) 5–15 MeV, and (3) 15–25 MeV (c.m.). The three functions $U_c(r)$ are displayed in Fig. 4. The first energy range includes the two bound states for which the first solution gives energies of -3.26 and -1.511 MeV for $l=0$ and $l=2$, respectively. The energy dependence of the phase shifts is accurately reproduced by the potentials for the respective energy ranges up to $l=5$. From Fig. 4 it is evident that the radial geometry of the V_1 component has little energy dependence, while the radial geometry for the V_2 component has a more significant dependence on energy. The differences between the solutions for V_2 are proportionally very large between 2 and 5 fm, which is why the inversion for the complete energy range was unsuccessful. The energy dependences of the V_1 component is not exactly linear as is clear from the variation in $\xi_{c\,1}$ which is -0.0076, -0.0058, and -0.0053 MeV^{-1} for the three solutions, respectively. The energy dependence thus decreases with increasing energy, as for the $p+\alpha$ case in Sec. III A 1. The values of $\xi_{c\,1}$ for the V_2 component are, in order, -0.041, -0.043, and -0.026 MeV^{-1}. The energy dependence for V_2 is therefore greater than in the $p+\alpha$ case, but for $n+{}^{16}$O, the V_2 potential is much smaller in magnitude and the coefficients $\xi_{c\,1}$ are less consistent.

The above results represent a uniform picture of the potential above and below zero energy, even though no energy independent form can be obtained for the potential shape.

IV. ENERGY DEPENDENT POTENTIALS FROM EMPIRICAL PHASE SHIFTS

A. Below the inelastic threshold

In a previous analysis [6], using techniques based on narrow energy bites, real parity dependent potentials were determined by fixed energy inversion of subthreshold empirical phase shifts for $n+\alpha$ and $p+\alpha$ scattering. The analysis was applied to two parametrizations of $p+\alpha$ phase shifts: the R-matrix parametrization, of Stammbach and Walter [26] and the effective range parametrization of Schwandt *et al.* [27]. Separate inversions were made for even and odd l values for each set of phase shifts for $l\leqslant 3$ in order to establish parity dependent potentials at selected energies from 12 to 20 MeV (lab). Potentials were later determined at much lower energies by increasing the weighting given to higher partial waves [28]. This procedure forces a reasonable fit for the d- and f-wave phase shifts as well as for the more strongly energy dependent s- and p-wave phase shifts. The central potentials for both $p+\alpha$ and $n+\alpha$ depend significantly on energy and this energy dependence is also evident when the potentials are expressed in the parity dependent form $V_1(r)+(-1)^l V_2(r)$. In this section, except where stated otherwise, energy and parity dependent potentials are established from phase shift parametrizations evaluated at intervals of 0.5 MeV over the energy range from 0.5 to 20 MeV, for $l\leqslant 3$. The present analysis compares potentials determined for both of the phase shift parametrizations.

1. Inversion of phase shift parametrizations

Inversion over a wide energy range does not yield an energy independent potential which accurately fits the $p+\alpha$ parametrized phase shifts. If all partial waves are weighted equally, a reasonable (smooth potential) fit is obtained only for the s- and p-wave phase shifts. Fitting all l closely induces pronounced radial oscillations in potentials. A typical set of values for $\delta_\kappa^{\rm inv}$ obtained from a smooth energy independent potential determined by inverting R-matrix phase shifts is shown in Fig. 5, together with the two sets of empirical phase shifts and the phase shifts obtained from an energy dependent potential (described below). The energy independent potential corresponds to a value for σ which is about 2.5 times that for the energy dependent potential. The $\delta_\kappa^{\rm inv}$ for the energy independent potential clearly fail to reproduce the phase shifts for higher l and higher energies. Energy independent potentials determined from the effective-range phase shifts yield slightly improved fits to the s- and p-wave phase shifts, but not to other l values. The fit to the d- and f-wave phase shifts can be improved with a judicious choice of the w_κ [defined in Eq. (3)], but this change leads to worse fits for low l.

The inclusion of just a linear energy dependence in each potential component produces an improved fit to the s- and p-wave phase shifts for both sets of phase shifts. To obtain a reasonable fit for all $l\leqslant 3$ simultaneously, the higher l values must be given an increased weighting. In fact, inverting with $w_\kappa(l=0,1)=1$ and $w_\kappa(l=2,3)=5$ gives a fit to the s and

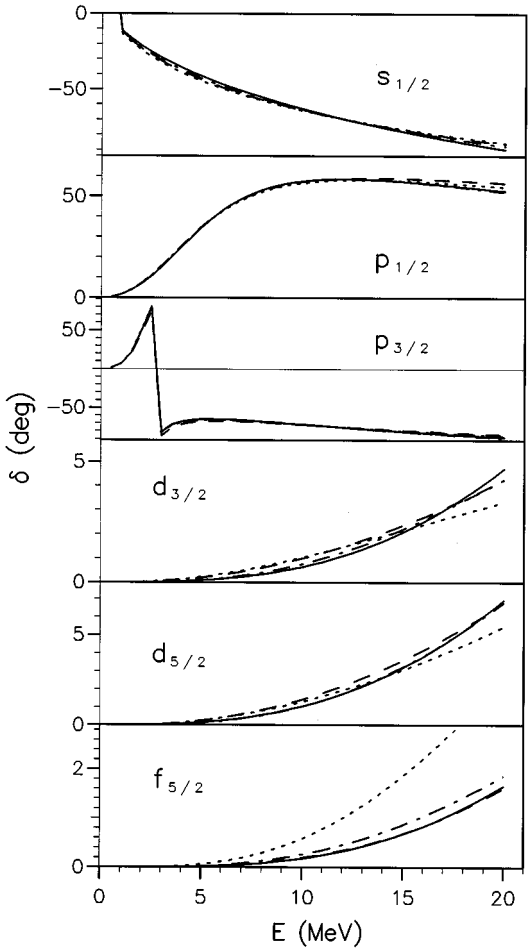

FIG. 5. For $p+\alpha$, R-matrix (solid lines), and effective-range (dashed lines) phase shifts for the partial waves $s_{1/2}$, $p_{1/2}$, $p_{3/2}$, $d_{3/2}$, $d_{5/2}$, and $f_{5/2}$. The dotted line is an energy independent fit and the dash-dotted line is the energy dependent fit RM(1) to the R-matrix phase shifts.

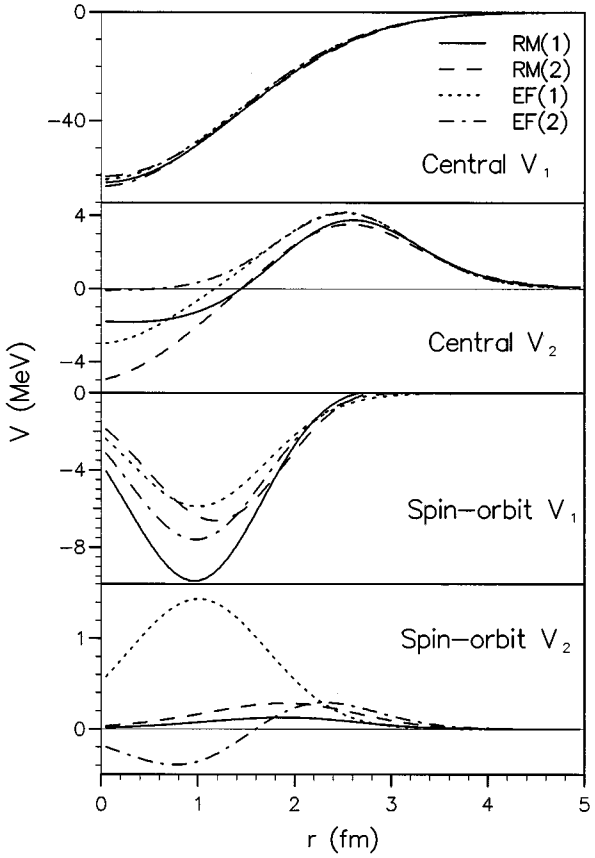

FIG. 6. Real zero energy potentials $U_c(r)$ deduced from sub-threshold empirical phase shifts for $p+\alpha$ scattering. Two inversions are from R-matrix fits [RM(1), solid line, and RM(2), dashed line] and two from effective range fits [EF(1), dotted line, EF(2), dot-dashed line].

p phase shifts equivalent to that obtained with $w_\kappa(l)=1$ (all l), while significantly improving the fit to the d and f waves. This effect probably arises because the energy dependent potentials which reproduce all l simultaneously are also a subset of the wider family of solutions which reproduce only the s- and p-wave phase shifts accurately. In Fig. 5, the fourth line (dash-dotted line) represents the $\delta_\kappa^{\rm inv}$ corresponding to the potential linearly dependent on energy obtained with $w_\kappa(l=2,3)=5$ from the R-matrix phase shifts. The difference between the latter phase shifts and the R-matrix parametrization is visible in Fig. 5 only for $l=3$ and is less than the difference between the two empirical parametrizations for most l and E. The increase in $w_\kappa(l)$ for the larger l significantly affects the parameters $\xi_{c\,1}$, particularly for the V_2 component.

Two energy dependent solutions, labeled RM(1) and RM(2), have been determined by inverting the R-matrix phase shifts and two solutions, labeled EF(1) and EF(2), by inverting effective range phase shifts. In all cases $w_\kappa(l=2,3)=5$ and comparable values of σ are obtained. The full potentials at zero energy, $U_c(r)$, are shown for all four solutions in Fig. 6. The volume integrals and root mean square (rms) radii are listed in the top part of Table III and the corresponding $\xi_{c\,1}$ are listed in the top part of Table IV. Although there are clear differences between the solutions in Fig. 6, certain features appear in all solutions and others are dependent on the particular set of target shifts. The largest component, the central V_1 term, is defined to within about 5 MeV for most of the radial range, but between about 1 and 3 fm the effective-range solutions are significantly shallower. Near $r=0$ the ambiguity between V_1 and V_2 can be observed and so the sign of $V_2(r)$ is not determined at small radii. A negative region for the central V_2 term at the nuclear center is consistent with both the previous fixed energy inversions [6,10] and with the energy dependent potentials determined from the RGM phase shifts in Sec. III A. The volume integrals and rms radii also illustrate the dependence of the solutions on the particular set of phase shifts.

The spin-orbit components are less well established. The rms radii are consistently smaller than for the central potentials, but the component V_1 is still not well determined between 1 and 2 fm. These differences do not appear to be related to the particular set of target phase shifts. The V_2 component is clearly much smaller and consequently very poorly defined. However, inversions which omit a V_2 spin-orbit term give higher values of σ.

The values of $\xi_{c\,1}$ tabulated in Table IV illustrate the expected decrease in the magnitude of the central potentials with energy, always much more rapid for V_2 than for V_1.

TABLE III. The volume integrals J_0, in MeV fm^3, and rms radii, in fm, for the four potential components determined by inversion from effective range, R-matrix phase shift parametrizations, or various sets of empirical phase shifts.

	Central V_1		Central V_2		Spin orbit V_1		Spin orbit V_2
$\mathbf{S}^{\text{tar}}$	J_0	$\langle r^2\rangle^{1/2}$	J_0	$\langle r^2\rangle^{1/2}$	J_0	$\langle r^2\rangle^{1/2}$	J_0
R matrix (1)	603.7	2.22	−153.1	3.22	58.4	1.34	−3.1
R matrix (2)	609.6	2.21	−147.2	3.27	52.0	1.43	−7.0
Effective range (1)	592.7	2.28	−161.5	3.06	49.4	1.80	−12.3
Effective range (2)	591.7	2.28	−165.0	3.05	54.5	1.62	−6.4
Stammbach and Walter	599.7	2.22	−165.0	3.10	54.9	1.62	−2.6
Schwandt *et al.*	595.3	2.28	−157.2	3.04	47.1	1.70	−13.6
Arndt *et al.*	532.2	2.05	−225.7	3.25	41.1	1.47	−21.3

The values of $\xi_{c\,1}$ for the central V_1 term depend strongly on the set of phase shifts, being of larger magnitude for the R-matrix solutions. A similar dependence is seen to a lesser degree for the central V_2 component. The values of $\xi_{c\,1}$ for the spin-orbit components have a much greater spread.

The inversion introduces a bias in favor of energies where the phase shifts have the largest energy dependence, so that the potential may be defined more accurately for certain energy regions than others. A way of measuring how the uncertainty in the potentials depends on energy is to study the volume integrals. The central V_1 potentials are then found to be most accurately defined at 10 MeV, in the center of the energy range. Strikingly, the variation in the volume integrals for $V_1(r)-V_2(r)$, i.e., the odd parity potential, is only 3 MeV fm^3 at zero energy whereas at 20 MeV the volume integral for the the sum of the two components, i.e., the even parity potential, is defined to a similar accuracy. Possibly the two p-wave resonances ensure that the odd parity potential is well determined at lower energies; the even parity potential is then determined more accurately at higher energies where the d-wave phase shifts are larger.

2. Precise form of energy dependence

Fine details of the energy dependence are likely to depend strongly on the particular set of phase shifts, as shown by the following calculations. Potentials, linearly dependent on energy, were determined by inversion over energy bites $E_{\text{cen}}\pm 1$ for both sets of phase shifts and for $E_{\text{cen}}=5$, 10, 15, and 20 MeV. Figure 7 shows the components $U_c(r)$ for one set of solutions, determined by inversion of the R-matrix phase shifts using the solution RM(1) as $V^{\text{srp}}(r)$, and the central V_1 component of $U_c(r)$ is remarkably independent of E_{cen}. However, the radial geometry of both V_2 components is strongly dependent on E_{cen}. For the R-matrix parametrization, these results are stable against changes in $V^{\text{srp}}(r)$. Very different results are found for effective range phase shifts. In this case solutions can be obtained which, when displayed on a graph similar to Fig. 7, show no discernible dependence on E_{cen} in any component except the small spin-orbit V_2 term.

The coefficients $\xi_{c\,1}$ obtained for the four E_{cen} are different for R-matrix and effective-range phase shifts. A clear pattern emerges only for the central potentials. For the R-matrix phase shifts $|\xi_{c\,1}|$ increases significantly with E_{cen} for both V_1 and V_2. For the effective-range phase shifts the dependence on E_{cen} is less clear, but overall $|\xi_{c\,1}|$ appears to decrease in magnitude with increasing E_{cen}.

3. Inversion directly from empirical phase shifts

Mixed case inversion can be applied to phase shifts determined separately at each energy (i.e., not involving parametrizations.) Parity dependent potentials, depending linearly on energy, have been determined from the discrete phase shifts of Stammbach and Walter [26], Schwandt *et al.* [27], and Arndt *et al.* [29]. Since the phase shifts depend less smoothly on energy than parametrized phase shifts, the resulting potentials are less well defined, but these potentials broadly verify the results of Sec. IV A 1. The volume inte-

TABLE IV. The coefficients $\xi_{c\,1}$ in MeV^{-1} for the four potential components determined by inversion from effective range, R-matrix phase shift parametrizations, and various sets of empirical phase shifts.

	Central V_1	Central V_2	Spin orbit V_1	Spin orbit V_2
$\mathbf{S}^{\text{tar}}$	ξ_{11}	ξ_{21}	ξ_{31}	ξ_{41}
R matrix (1)	−0.0065	−0.0142	0.0055	−0.00014
R matrix (2)	−0.0064	−0.0119	0.0097	−0.0057
Effective range (1)	−0.0043	−0.0119	0.0032	0.0344
Effective range (2)	−0.0045	−0.0123	0.0089	−0.00039
Stammbach and Walter	−0.0066	−0.0155	0.0153	0.0097
Schwandt *et al.*	−0.0047	−0.0111	−0.0006	0.0345
Arndt *et al.*	−0.0012	−0.0317	−0.0123	0 .0323

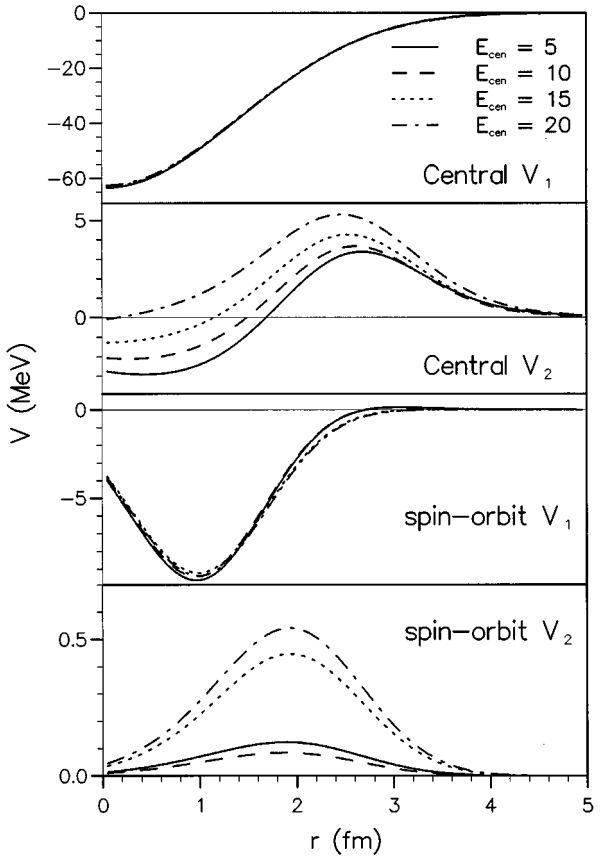

FIG. 7. Zero energy potentials $U_c(r)$ determined from subthreshold empirical phase shifts for $p+\alpha$ scattering. The four solutions are all determined from the R-matrix phase shifts by energy dependent inversion over the energy intervals $E_{\rm cen}\pm 1$ MeV, with $E_{\rm cen}=$ 5 MeV (solid lines), 10 MeV (dashed lines), 15 MeV (dotted lines), and 20 MeV (dot-dashed lines).

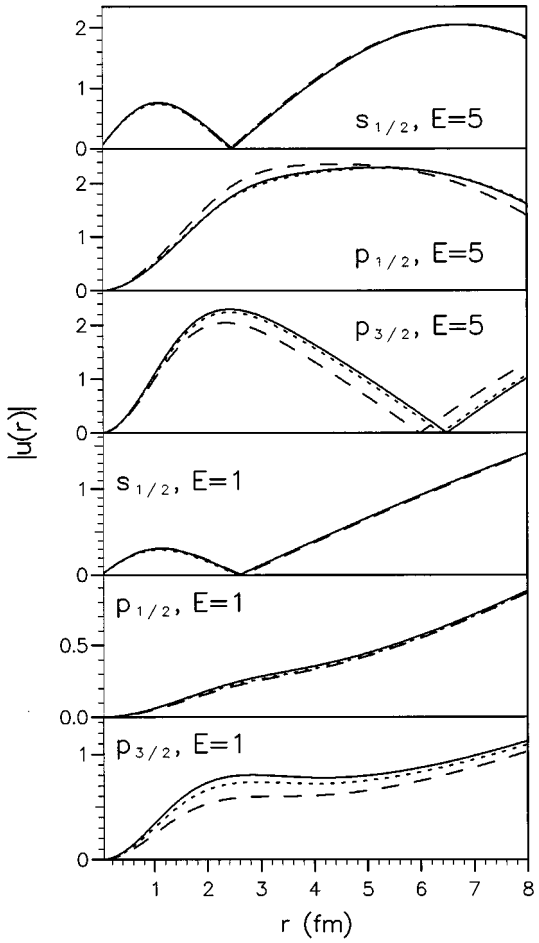

FIG. 8. The wave functions $u_\kappa(r)$ determined for $p+\alpha$ for the partial waves $s_{1/2}$, $p_{1/2}$, and $p_{3/2}$ at 1 MeV (lower three panels) and 5 MeV (upper three panels). The solid lines represent $u_\kappa(r)$ calculated from potentials found from fixed energy inversion at the ''correct'' energy, e.g., 5 MeV in the upper three panels. The dashed lines represent $u_\kappa(r)$ for potentials at the ''wrong'' energy, e.g., at 5 MeV in the lower three panels. The dotted line represents $u_\kappa(r)$ calculated from an energy dependent potential and is evaluated at the respective correct energy.

grals and rms radii of $U_c(r)$ and the values of $\xi_{c\,1}$ are listed in the lower parts of Tables III and IV which confirm the consistency of our procedure. Further details are given in Ref. [21].

4. Wave functions from fixed energy and energy dependent analyses

Analysis of nuclear reactions often exploits potential models to calculate wave functions for use in the reaction model. These wave functions will be inaccurate for small radii due to nonlocality, but can also sometimes have large errors in the asymptotic radial region. This is most likely to occur where the potential is determined for a single energy but used at a different energy, the underlying potential being strongly energy dependent. These effects arise for $p+\alpha$ scattering at low energies where there are p-wave resonances.

Wave functions $u_\kappa(r)$ corresponding to three parity dependent potentials for $p+\alpha$ are presented for the $s_{1/2}$, $p_{1/2}$, and $p_{3/2}$ partial waves in Fig. 8. Two of the potentials are energy independent, determined from effective-range parametrized phase shifts of Schwandt *et al.* for narrow energy bites at $E=1$ and 5 MeV. The third is the energy dependent potential EF(1). The wave functions in the top three panels of Fig. 8 are calculated at 1 MeV and in the lower three panels at 5 MeV. In each panel, one of the wave functions is calculated with a potential determined to reproduce the phase shifts at that energy correctly and one wave function is calculated using the potential obtained for the other energy. The energy dependent potential is evaluated at the appropriate energy in each case. Clearly, energy dependence in the potentials is most important for the p-wave functions. The wave functions calculated at 1 MeV from the 5 MeV potentials, or vice versa, have significant errors for $r>1$ fm. By contrast, wave functions for the s waves and also $l\geqslant 2$ (not shown), where there are no resonant effects, are calculated accurately using potentials for the ''wrong'' energy.

B. Empirical *S* matrices above the inelastic threshold

Various phase shift analyses have been made for $p+\alpha$ scattering for energies above the inelastic threshold. For energies up to 50 MeV beyond the threshold energy at 23 MeV, the most comprehensive analyses are those of Plattner

TABLE V. The coefficients p, σ, and $\xi_{c\,1}$, in MeV^{-1}, for four potentials determined by inversion from the various sets of empirical phase shifts. Except for the solutions number (4) in each case, the values of $\xi_{c\,1}$ are for a linear energy dependence in the real potentials. For solutions (4) coefficients are given for both the real potential expansion and for a term in E^2 in the imaginary components.

Inversion	p	σ	Central V_1	Central V_2	Spin orbit V_1	Spin orbit V_2
Inversion from S_κ of Houdayer *et al.*						
(1)	1	0.522	−0.0023	−0.0159	−0.0055	−0.0048
(2)	1	0.423	−0.0030	−0.0135	0.1346	−0.0095
(3)	0.5	0.468	−0.0019	−0.0153	−0.0072	−0.0087
(4) Real		0.410	−0.0021	−0.0159	−0.0060	−0.0098
(4) Imag	1		−0.0021	−0.0034	−0.0020	−0.0020
Inversion from S_κ of Plattner *et al.*						
(1)	1	0.340	−0.0010	−0.0170	−0.0093	−0.0007
(2)	1	0.279	−0.0025	−0.0147	0.0499	−0.0090
(3)	0.5	0.332	−0.0003	−0.0166	−0.0093	−0.0119
(4) Real		0.292	−0.0006	−0.0163	−0.0093	−0.0078
(4) Imag	1		−0.0021	−0.0035	−0.0019	−0.0020
Inversion from S_κ of Burzynski *et al.*						
(5)	1	0.810	−0.0054	−0.0109	0.0002	−0.0028
(6)	0.5	0.730	−0.0053	−0.0109	0.0004	−0.0028
(7)	0.0	0.788	−0.0053	−0.0108	0.0005	−0.0028
(4) Real		0.748	−0.0054	−0.0133	−0.0032	−0.0070
(4) Imag	1		−0.0015	−0.0027	−0.0028	−0.0029

et al. [13], Houdayer *et al.* [14], Burzynski *et al.* [15], and Saito [16]. All these empirical phase shifts have significant fluctuations in the energy dependence of each partial wave, which is particularly evident in the absorption coefficients. The first three S-matrix sets have the more regular energy dependence so that these, and not the S matrix of Saito [16], are considered. There are, however, distinct differences between these three data sets [15], which may be due to systematic errors in the phase shift analyses.

The phase shift sets cover different energy ranges, i.e., ~19 to ~40 MeV for the analysis of Plattner *et al.*, which includes phase shifts determined for subthreshold energies, ~23 to ~50 MeV for the analysis of Houdayer *et al.* and ~30 to ~70 MeV for the analysis of Burzynski *et al.* The S matrix of Houdayer *et al.* covers the energy range above the inelastic threshold most comprehensively.

Close to the inelastic threshold, the $d_{3/2}$ resonance is a dramatic feature affecting the behavior of both $|S|$ and $\arg(S)$ and the very strong effect on $|S|$ persists to energies well above the resonance energy [13]. This resonance is not single particle in character, and so we do not attempt to fit the resonance phase shifts with a local potential. In the calculations based on the S matrix of Houdayer *et al.* the empirical $d_{3/2}$ phase shift for $|S|$ up to 35 MeV is replaced with the background term in the R-matrix fit of Plattner *et al.* The inversion of the S matrix of Plattner *et al.* uses this substitution for both $|S|$ and $\arg(S)$. No substitution is made in the calculations based on the S matrix of Burzynski *et al.* Anomalous behavior is also found in $|S|$ for the $p_{1/2}$ S-matrix elements of Houdayer *et al.*, which may be due to broad $p_{1/2}$ states. Except where otherwise stated, the $p_{1/2}$ $|S|$ of Houdayer *et al.* is replaced with the corresponding empirical $p_{3/2}$ $|S|$ to avoid the possibility of spurious effects in the inversion calculations due to this anomaly.

Above the inelastic threshold the $p+\alpha$ potential has eight components if the complex, central, and spin-orbit terms are all parity dependent. However, energy dependent inversion requires only four more free parameters, assuming a linear energy dependence in the real components, because the imaginary components vanish at the threshold energy. Although the radial basis for each component is kept small, not all of these free parameters are well determined from the empirical data. The large component of ''noise'' in the S-matrix data severely limits the accuracy to which this data can be reproduced by inversion and the lack of known uncertainties in the target S-matrix prohibits proper error estimation. Uncertainties are assessed by applying alternative inversion parameters and choices for the starting reference potential.

In Secs. IV B 1 and IV B 2 we briefly compare potentials for the Houdayer and Burzynski S-matrix sets. For an account of similar studies involving the S-matrix of Plattner *et al.*, see Ref. [21]; the numerical results are included in Tables V and VI. An overall comparison of all the solutions, including a comparison with the subthreshold solutions, is made in Sec. V.

1. Inversion from the S matrix of Houdayer et al.

A considerable improvement in the fit over that obtained from energy independent potentials follows from the introduction of a linear energy dependence into both the real and imaginary components. However, some trends in the energy dependence of $|S_\kappa^{\mathrm{tar}}|$ are not well reproduced with a linear energy dependence in the imaginary component. Nonlinear energy dependence of the imaginary potentials is therefore considered. There is no empirical parametrization of these phase shifts so direct inversion is used as in Sec. IV A 3.

TABLE VI. The volume integrals J_0, in MeV fm^3, and rms radii, in fm, for the central and spin-orbit V_1 and V_2 components of the four solutions determined by inversion from the various empirical S-matrix sets. The volume integrals are given for the real potentials at $E=0$ and for imaginary components at $E=30$. Where the rms radii could not be calculated due to long range radial oscillations about $V(r)=0$, the value is marked with a hyphen.

	Central V_1		Central V_2		Spin orbit V_1		Spin orbit V_2
			The real components, at $E=0$				
Solution	J_0	$\langle r^2\rangle^{1/2}$	J_0	$\langle r^2\rangle^{1/2}$	J_0	$\langle r^2\rangle^{1/2}$	J_0
Inversion of S_κ of Houdayer *et al.*							
(1)	550.3	2.38	−231.2	2.90	67.3	1.89	−25.8
(2)	542.2	2.38	−218.4	2.47	4.85	2.52	−60.3
(3)	543.3	2.33	−230.3	2.63	81.0	1.71	−24.5
(4)	545.1	2.33	−240.9	2.66	72.4	1.76	−30.6
Inversion of S_κ of Plattner *et al.*							
(1)	548.9	2.44	−242.9	2.63	72.0	1.74	−21.3
(2)	555.9	2.44	−239.2	2.31	9.52	2.69	−61.6
(3)	540.5	2.42	−254.7	2.52	84.6	1.58	−20.3
(4)	544.1	2.41	−253.9	2.51	77.8	1.69	−25.9
Inversion of S_κ of Burzynski *et al.*							
(4)	607.8	2.28	−205.2	2.07	76.8	1.82	−10.9
(5)	591.1	2.33	−176.0	2.87	59.2	1.84	−10.0
(6)	591.9	2.34	−170.8	2.81	59.1	1.83	−9.60
(7)	594.3	2.36	−159.2	2.69	59.6	1.82	−8.73
			The imaginary components, at $E=30$ MeV				
	J_0	$\langle r^2\rangle^{1/2}$	J_0	$\langle r^2\rangle^{1/2}$	J_0	$\langle r^2\rangle^{1/2}$	J_0
Inversion of S_κ of Houdayer *et al.*							
(1)	34.4	3.04	13.0	2.86	13.7	—	12.9
(2)	35.5	2.66	15.8	2.48	5.09	—	4.5
(3)	55.1	2.93	17.1	2.71	16.3	—	18.1
(4)	43.4	2.89	21.8	2.73	19.2	—	18.2
Inversion of S_κ of Plattner *et al.*							
(1)	43.2	3.27	23.5	3.19	12.9	—	10.8
(2)	43.2	3.06	25.33	3.10	4.86	—	3.09
(3)	48.1	3.05	20.0	3.10	17.8	—	19.0
(4)	46.3	3.40	27.8	3.62	19.3	—	16.8
Inversion of S_κ of Burzynski *et al.*							
(4)	35.6	2.86	17.0	1.45	17.3	—	16.0
(5)	26.7	3.19	6.4	1.87	0.95	—	0.34
(6)	56.6	3.17	112.2	—	2.1	—	0.6
(7)	95.2	3.00	13.8	—	4.3	—	1.5

Four distinct solutions have been determined, all with real components linearly dependent on energy. The energy dependence of the imaginary components for the solutions are (1) linear energy dependence for both real and imaginary components, (2) as in (1) but with the SVD tolerance decreased to yield a significantly lower value of σ and correspondingly a more oscillatory potential, (3) energy dependence of the imaginary components with $p=0.5$, and (4) energy dependence of the imaginary components with both the linear term and the second order term $\xi_{c\,2}E^2$. The same radial basis has been used for all four cases and the values of σ obtained for each case are listed in Table V. A markedly less accurate fit, i.e., $\sigma\sim 0.7$, was found with $p=2$ in a further calculation similar to case (3).

In Figs. 9 and 10 the $S_\kappa^{\rm inv}$ resulting from the four cases are compared with the empirical S-matrix elements of Houdayer *et al.* for the lowest l values. The energy dependence of $S_\kappa^{\rm inv}$ is very consistent for the four solutions for most partial waves. The empirical $\arg(S_\kappa)$, particularly the s and p waves, are generally well reproduced by inversion, but the $|S_\kappa^{\rm tar}|$ are less well reproduced. The energy dependence of $|S|$ for the s, $p_{3/2}$, $d_{5/2}$, and f waves is reasonably well predicted using the simple linear energy dependence, although solution (4), with the additional term in E^2, provides a better description at the highest energies. However, a nonlinear energy dependence with $p=0.5$, case (3), leads to a marginally better description of the very strong absorption in the $d_{3/2}$ phase shifts. No conclusive evidence is therefore found for a nonlinear energy dependence in the imaginary potential.

The real parts of the four solutions at $E=0$, $U_c(r)$, are shown in Fig. 11. The central V_1 potential is the best defined, with solution (2) differing most from the other solutions. However, solution (2) has a rather irregular radial depen-

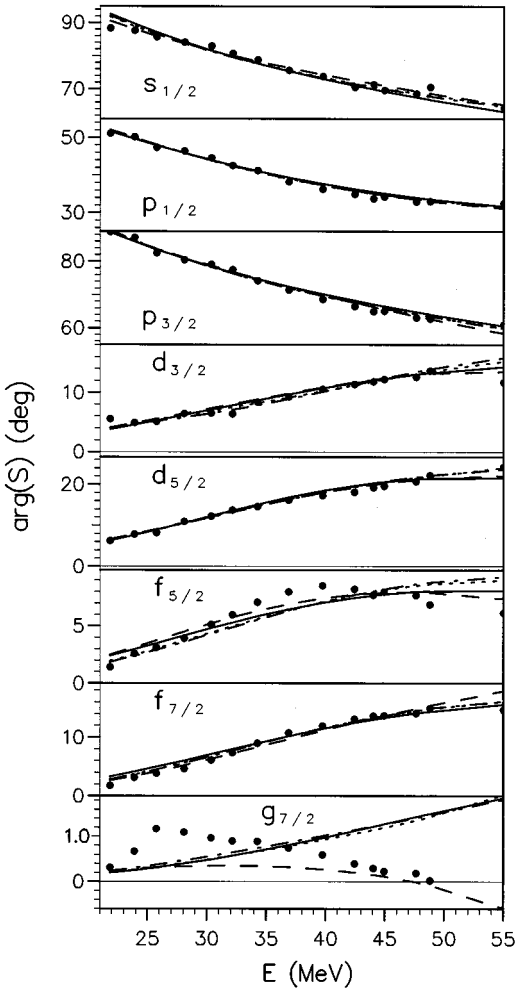

FIG. 9. For $p+\alpha$ above the inelastic threshold, $\arg(S_{lj})$ for $l \leqslant 3$ and $g_{7/2}$. The empirical values of Houdayer *et al.* (solid dots) are compared with $\arg(S_{lj})$ for the four solutions described in the text, (1) solid lines, (2) dashed lines, (3) dotted lines, and (4) dash-dotted lines.

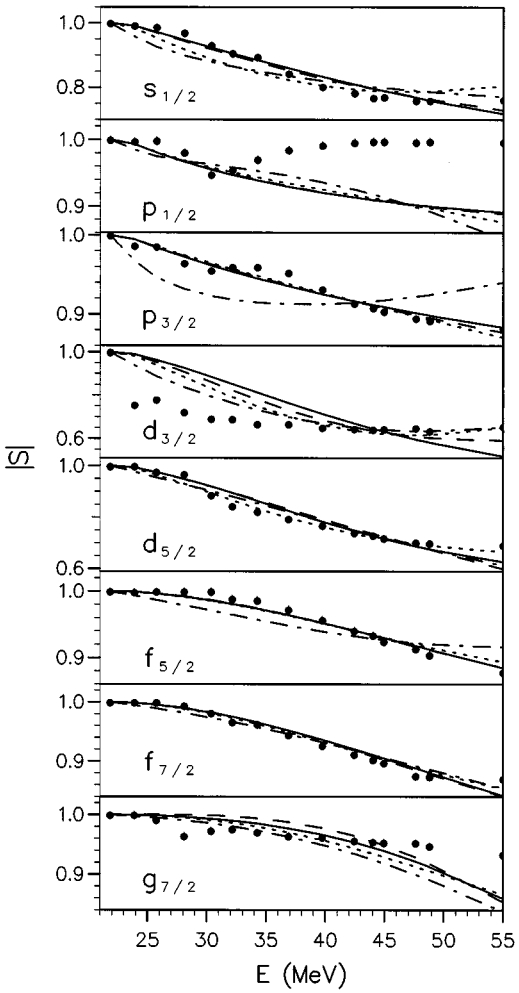

FIG. 10. As in Fig. 9 for $|S_{lj}|$.

dence which is probably due to over-fitting and can be discounted. Solutions (1), (3), and (4) closely agree for $r>1.5$ fm and $r<4$ fm and are greater in magnitude than the subthreshold solutions shown in Fig. 6. The parameters $\xi_{c\,1}$ in Table V for solutions (1), (3), and (4) are reasonably consistent for the central potentials and a linear energy dependence in the real potentials can be considered fairly well established for the S matrix of Houdayer *et al.* The rms radii and volume integrals at $E=0$ are listed in Table VI and are reasonably well defined for the central V_1 component. An even closer agreement is found for the volume integrals at 30 MeV. For the real central V_2 component both the volume integrals and rms radii, even without solution (2), have a slightly larger spread in values. The rms radius for the central V_2 component is still significantly larger than that of the V_1 component.

A similar degree of consistency is found for the real spin-orbit potentials to that found for the real central potentials. Discounting the overdetermined and anomalous solution (2) the solutions of $V_1(r)$ agree with the potentials calculated at subthreshold energies. The parity dependent (V_2) spin-orbit potentials appear to be an order of magnitude greater than the subthreshold solutions, but this component is not well determined. However, the parameters $\xi_{c\,1}$, listed in Table V, now show a decrease in the potential with energy for both V_1 and V_2 terms. The spin-orbit potential is again more accurately determined at higher energies, as found in the volume integrals. The rms radius of the spin-orbit V_1 component is considerably smaller than the radius of both real central potentials for all solutions except (2).

The radial components $U_c(r)$ of the imaginary potentials for the four solutions, for which $E'_{\rm ref}=30$ MeV, are shown in Fig. 12. The magnitudes of the central components are reasonably well established, with potential depths of at least ~ 1.0 and ~ 0.5 MeV for the V_1 and V_2 components, respectively. The rms radius is slightly smaller for V_2 than for V_1 and the volume integrals are much smaller for the V_2 terms. The difference between the potentials increases with energy so that, at 50 MeV, the volume integrals are ~ 120 and ~ 40 MeV fm^3 for V_1 and V_2, respectively. The decrease in the magnitude of both components towards the nuclear center is necessary to reproduce $|S_\kappa^{\rm tar}|$ for the s wave. This partial wave is the most sensitive to the potential near the nuclear center and is much less absorbed than the d waves. However, the imaginary components have an ambiguity near the nuclear center, similar to that noted for the real components.

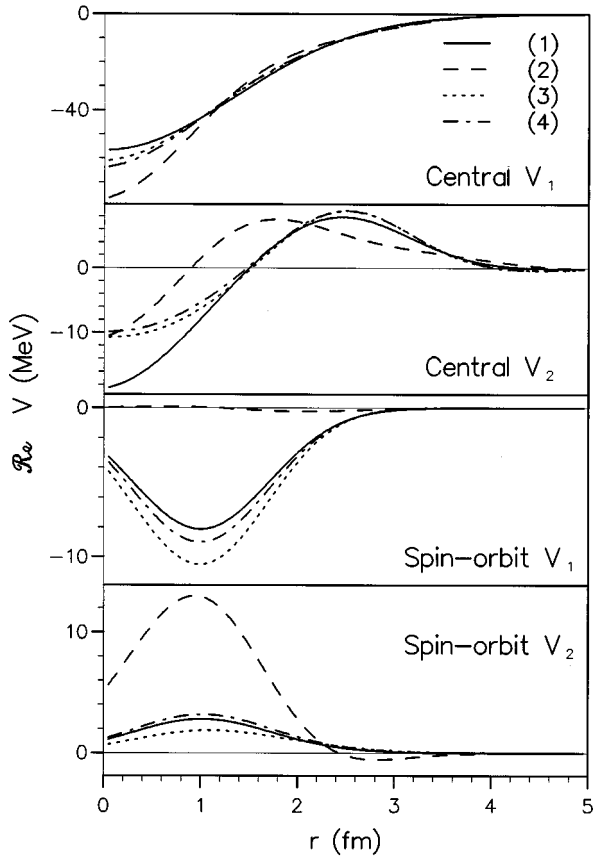

FIG. 11. For $p+\alpha$ above the inelastic threshold, the real potentials evaluated at $E=0$ [i.e., $U_c(r)$] for the four solutions resulting from inversion on the S matrix of Houdayer *et al.*, (1) solid lines, (2) dashed lines, (3) dotted lines, and (4) dash-dotted lines.

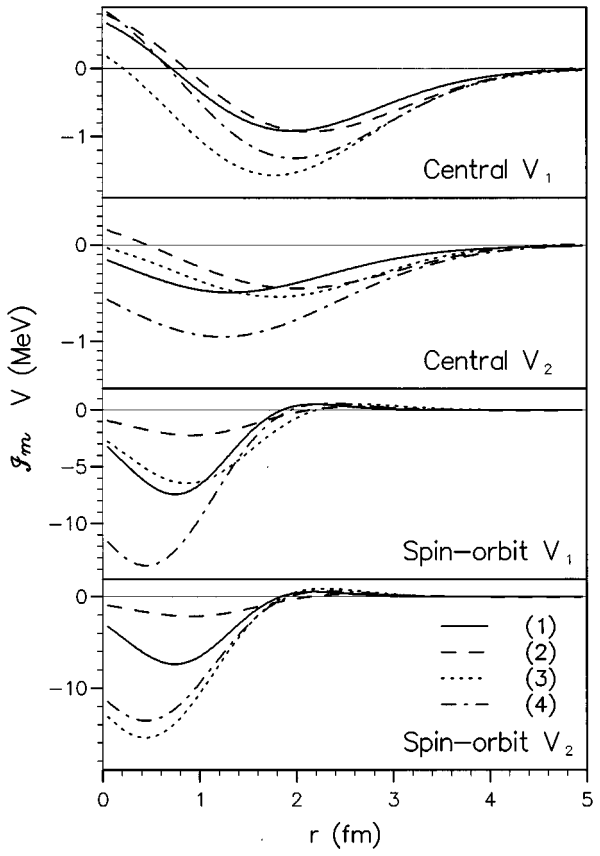

FIG. 12. As in Fig. 11 for the imaginary potentials, evaluated at $E'_{\rm ref}=30$ MeV.

The imaginary spin-orbit components are not very well determined by inversion, although omitting them from the inversion results in a distinctly higher σ. The large magnitude at small radii, i.e., $r<2$ fm (see Fig. 12), is not reflected in the volume integrals. The rms radii cannot be directly calculated for these potentials due to the potential oscillations. These potentials are effectively established by the large differences between $|S_\kappa|$ for $d_{3/2}$ and $d_{5/2}$, together with the imposed requirement that $|S_\kappa|$ is equal for the two p waves and are probably not realistic.

Direct inversion of the empirical $p_{1/2}\,|S_\kappa|$ shows that only small differences in the potentials result from the substitution for $|S_\kappa|$, only the imaginary central components at small radii, i.e., $r<2$ fm, being noticeably modified. At larger radii the corrections are always less than the differences between the original solutions. No significant changes are introduced in the real components, the energy dependent parameters, or the imaginary spin-orbit components.

2. Inversion from the S matrix of Burzynski et al.

The S-matrix set of Burzynski *et al.* covers a wider energy range than those of Plattner *et al.* or Houdayer *et al.* and is less influenced by the $d_{3/2}$ resonance. It should therefore provide a more reliable determination of the energy dependent potential. The values of σ and the corresponding $\xi_{c\,1}$ for three solutions (labeled 5, 6, and 7), each with a different form of energy dependence in the imaginary components, are listed in Table V, as well as the parameters of a solution obtained using the solution (4) of Sec. IV B 1 as the starting reference potential. For one solution, (7), the imaginary potential is independent of energy. The volume integrals and rms radii of $U(r)$ for all four new solutions are listed in Table VI. The σ values are generally higher than for the other S-matrix sets mainly because of the greater fluctuations in the energy dependence of the phase shifts of Burzynski *et al.*

The potentials $U_c(r)$ for the real components of the solutions (4)–(7) are shown in Fig. 13. These solutions are generally consistent in all components. The difference between solution (4), consistent with the solutions of Sec. IV B 1, and the other solutions for the central components is of an oscillating radial form, typical of the oscillations due to overfitting. The volume integrals at zero energy for the four solutions reflect the consistency in the radial potentials, particularly in the rms radius of the central V_2 component and the volume integral of the spin-orbit V_1 component. The volume integrals of the central V_1 term are significantly greater in magnitude than the values for the S matrix of Houdayer *et al.*, while the volume integrals for V_2 are less in magnitude. However, the rms radii obtained using the S matrix of Burzynski *et al.* have very similar values to those obtained for the other S-matrix sets. At a laboratory energy of 30 MeV the spread of volume integrals of both potential components almost overlaps with that for the S matrix of

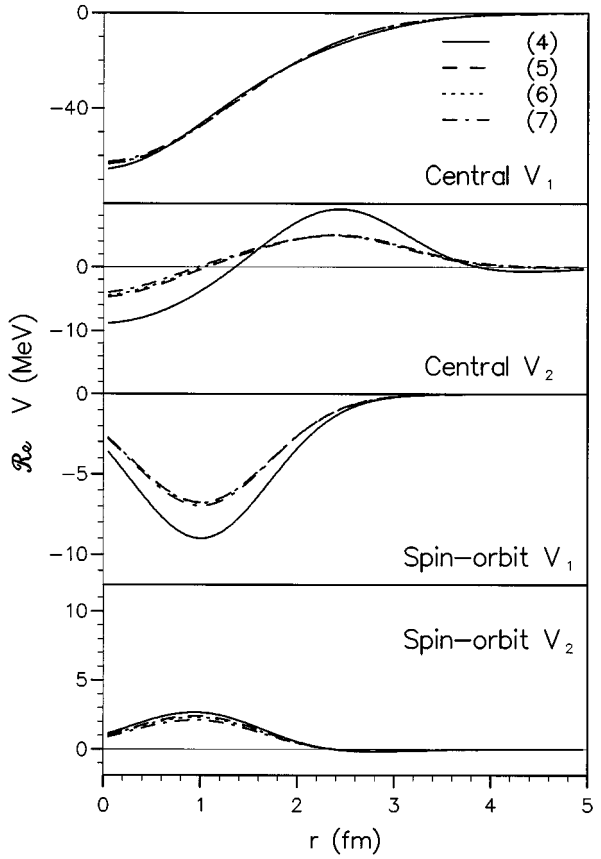

FIG. 13. For $p+\alpha$ above the inelastic threshold, real potentials evaluated at $E=0$ [i.e., $U_c(r)$] for the four solutions resulting from inversion on the S matrix of Burzynski *et al.*, (4) solid lines, (5) dashed lines, (6) dotted lines, and (7) dash-dotted lines.

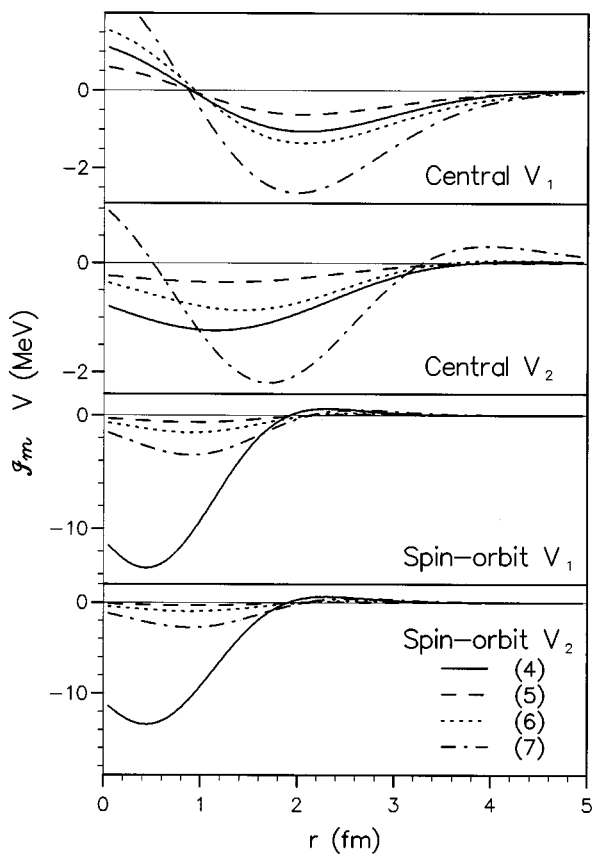

FIG. 14. As in Fig. 13 for the imaginary potentials, evaluated at $E'_{\rm ref}=30$ MeV.

Houdayer *et al.* The similarities in the radial form between the solutions (4)–(7) are also reflected in the $\xi_{c\,1}$ for the V_2 component listed in Table V. Excluding solution (4), there is an excellent agreement between all the solutions. For the V_1 term, $\xi_{c\,1}$ is significantly greater in magnitude than that for the S matrix of Houdayer *et al.*, while for the V_2 term, $\xi_{c\,1}$ is significantly less in magnitude than that previously calculated. The spin-orbit potentials show a greater consistency in energy dependence than those for other S-matrix sets. The radial dependence of the spin-orbit potentials agrees reasonably with the inversions from the S matrix of Houdayer *et al.*

In Fig. 14, $U_c(r)$ is presented for the imaginary components of the four solutions, evaluated at 30 MeV. The energy dependence of the imaginary potential is expected to decrease at energies significantly above the inelastic threshold and our results may reflect this behavior. The solution (6) with $p=0.5$ has the lowest value of σ, while σ for the energy independent solution (7) is lower than for the solution (5), linearly dependent on energy. The spread in the central potential solutions arises partly because the potentials are evaluated at the lower end of the energy range of the inversion. At 50 MeV, in the center of the energy range of the inversion, the volume integrals for the central V_1 component agree more closely than at 30 MeV. The volume integrals for the other potential components show no obvious consistency at 50 MeV. Apart from solution (4), the imaginary spin-orbit components are much smaller than those obtained from the S matrices of Houdayer *et al.* or Plattner *et al.*

V. OVERALL $p+$ ALPHA POTENTIAL

A. Real components

In the preceding sections a good representation of the empirical phase shifts, above and below the inelastic threshold, has been obtained with a local potential for which the magnitude of each component is energy dependent. A linear dependence on energy, $V_c(E,r)=U_c(r)(1+\xi_{c\,1}E)$, generally appears adequate for the real components. Only the phase shift parametrizations for the subthreshold energy range are sufficiently accurate to determine details of the higher order terms in the energy dependence. However, the two subthreshold $p+\alpha$ parametrizations give inconsistent predictions for any energy dependence in the potential shape. At energies above the inelastic threshold the S matrices are not sufficiently smooth in energy to establish any second order terms.

Parity dependent potentials are found necessary for all cases in Secs. III and IV and the real components $U_c(r)$ are illustrated in Figs. 6, 11, and 13. Overall, the central potentials have a well-established radial geometry for energies both above and below the inelastic threshold. The central V_1 component is approximately Gaussian in shape with a depth of about 60 MeV at zero energy and the central V_2 components all contain a maximum at $r\sim 2-2.5$ fm, which

generally results in a change in sign around $r \sim 1-1.5$ fm. For both central components the magnitude of $V_c(E,r)$ decreases with energy and the energy dependence is much larger for the V_2 component. The sign of V_2 is such that the odd parity term has a much longer range than the even parity term, as previously found in Ref. [6].

Quantitative details of the real potential components $V_c(E=0,r)$ are listed in Tables III–VI. Below the inelastic threshold, the central components are well defined in terms of the volume integrals, rms radii, and energy dependence parameters $\xi_{c\,1}$. Above the inelastic threshold there are significant variations in the parameters determined from different S-matrix sets. The potentials determined from the S matrix of Burzynski *et al.* are closest to the subthreshold potentials in terms of $\xi_{c\,1}$ and the volume integrals. This agreement is most obvious for the central V_1 component, although the rms radii deduced at the higher energies are greater than the corresponding values obtained below the inelastic threshold. The magnitude of the volume integrals of the central V_2 component for the S matrix of Burzynski *et al.* are less than the values for the S-matrix sets of Houdayer *et al.* and Plattner *et al.*, but are still greater than for the subthreshold solutions. The central V_2 rms radius is found to be smaller for the potentials above the threshold energy. These results are partially verified by the systematics obtained in the inversion from the RGM phase shifts in Sec. III A 1. However, the RGM solutions give a considerably greater variation with $E_{\rm cen}$ for the rms radii of the RGM potentials than that found for empirical potentials. The energy dependence of the parity independent real potential is very similar to that of the best global empirical nucleon-nucleus potential, the ''CH89'' potential of Ref. [30]. Expressing the energy dependence of the CH89 real central volume integral in the form $J(E)=J_0(1+\xi_{11}E)$ gives $\xi_{11}=-0.005\,37$ MeV^{-1} for $p+{}^4$He. This value agrees well with that calculated both from the S matrix of Burzynski *et al.* and from the subthreshold phase shifts.

The spin-orbit potentials are less well determined from the empirical phase shift analyses, but the term for V_1 is clearly negative and has a minimum of ~ -6 to -10 MeV at 1 fm for almost all solutions. Below the inelastic threshold the spin-orbit V_1 component increases in magnitude with energy for most solutions, as predicted by the RGM plus inversion calculations. The calculations for energies above the inelastic threshold give spin-obit components which either decrease with energy or are nearly energy independent.

Energy dependent potentials obtained from empirical S-matrix sets can only be considered reliable when evaluated at energies inside the energy range of the empirical data. The threshold energy of 23 MeV is the most suitable energy at which to compare the solutions for energies above and below the inelastic threshold. In Fig. 15, real components of $V_c(E=23,r)$ are shown for selected solutions from Sec. IV. The central V_1 component is the most consistently determined, for which the potential determined from the S matrix of Arndt *et al.* differs most from the other solutions. For the central V_2 component, the solutions all have the same basic shape, but differ widely in magnitude. The extreme cases are now those obtained from the phase shifts of Arndt *et al.* and from the S matrix of Houdayer *et al.*, which are very similar to the solutions obtained from the S matrix of Plattner *et al.*

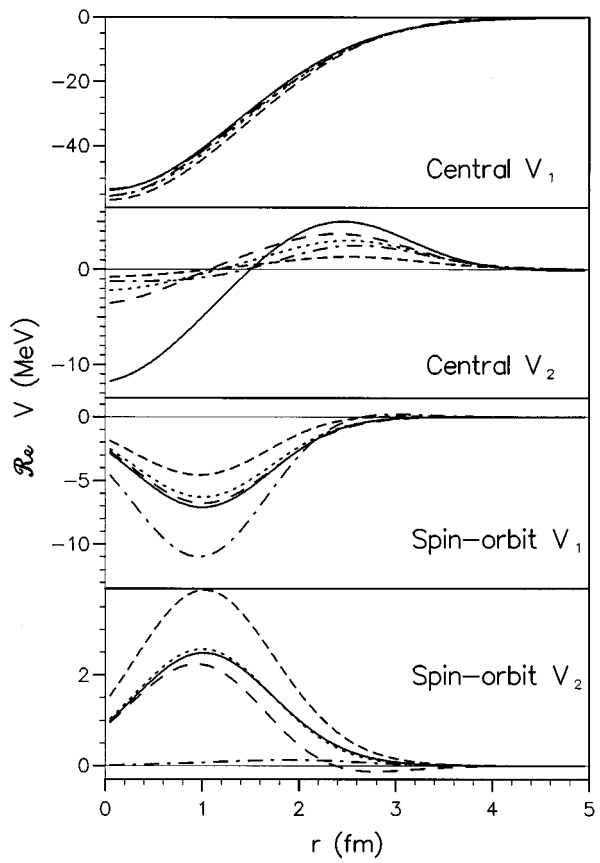

FIG. 15. For $p+\alpha$, real energy dependent potentials evaluated at $E=23$ MeV. The potentials, selected from Secs. IV A and IV B are solution (1) of Sec. IV B 1 (solid line), solution (5) of Sec. IV B 2 (long-dashed line), EF(1) (dotted line), RM(1) (dot-dashed line), and the solution obtained from the phase shifts of Arndt *et al.* (short dashed line).

For the spin-orbit potentials, including the small V_2 component, the widest discrepancies are found for the solution RM(1). Overall, the two solutions closest in agreement for all four components are the potential obtained from the data of Burzynski *et al.* and the solution EF(1).

Evaluated at 65 MeV, the energy dependent solution obtained from the data of Burzynski *et al.* is very similar to a solution previously obtained by fixed energy inversion [10], particularly for the V_1 central and spin-orbit terms. At this higher energy the solutions based on the data of Houdayer *et al.* and Plattner *et al.* are not valid due to the large energy dependence of the central V_2 term.

B. Imaginary components

The $|S_\kappa|$ for the three sets of S matrices determined for energies above the inelastic threshold fluctuate considerably with energy and, consequently, the imaginary part of the $p+\alpha$ potential is not well determined. Further uncertainties arise in the treatment of the $d_{3/2}$ and the $p_{1/2}$ S-matrix elements. The $|S|$ for these partial waves are difficult to reproduce by inversion, while the $d_{3/2}$ partial wave is crucial in the determination of the imaginary components. Both components of the central imaginary potential are small, $\sim 1-2$ MeV maximum in magnitude for a scattering energy of 30 MeV. The spin-orbit components have a clearly smaller rms

radius but otherwise are poorly determined. It is difficult to make a direct comparison between the potentials determined from the various empirical S-matrix sets due to the different forms of energy dependence used in the solutions. One persistent feature seen in $U_c(r)$ for both imaginary central components is a reduction in the potential magnitude towards the nuclear center. For the V_1 term this creates a generative region for small radii. This feature does not break unitarity and arises predominantly because the absorption is much greater for the d-wave phase shifts than for the lower l values. Its origin probably lies in the underlying nonlocality of the real potential.

For the imaginary central V_1 component, the energy dependent potentials evaluated at 65 MeV, $V_c(E=65,r)$, agree well with the corresponding component obtained from fixed energy inversion at 65 MeV, with allowance for the uncertainty of the solutions in Fig. 12. At 65 MeV, this component has a minimum of ~ -6 MeV close to 2 fm for most solutions. The central V_2 component at this energy has a greater spread but most of solutions agree around 2 fm.

Not surprisingly, the spin-orbit potentials determined from the S matrix of Houdayer *et al.* and Plattner *et al.* evaluated at 65 MeV show almost no agreement with those obtained from the S-matrix of Burzynski *et al.*

The S-matrix sets just above the inelastic threshold can be fitted quite well with imaginary components which depend linearly on energy and become zero at the threshold energy. However, the S-matrix set of Burzynski *et al.* covers a higher energy range and appears to be more accurately reproduced either with a reduced energy dependence, $\propto E^{1/2}$, or with energy independent imaginary components. The fits to $|S_\kappa|$ just above threshold are also unsatisfactory for some partial waves, the small $d_{3/2}$ $|S|$ presenting a problem to the inversion. Either an improved energy expansion $F_c(E)$ must be found or the potential geometry must be permitted to depend on energy. Unfortunately, the erratic energy dependence of $|S|$ prohibits use of energy bite techniques which otherwise offer the best way to investigate this problem.

C. Evaluation of the resonating group model

Energy dependent inversion of phase shifts derived from RGM yields a systematic pattern of potential components with distinctive features which are present over a wide energy range. Both the radial shape and the energy dependence of these potentials can now be compared with empirical solutions, providing an improvement upon previous comparisons [9,10]. This comparison is arguably more meaningful than direct fits of RGM to experiment since the RGM calculations necessarily employ somewhat schematic effective N-N interactions.

The sign and general radial properties of the central and spin-orbit V_1 components determined from RGM phase shifts in Sec III A 2, and in particular the central V_2 term, agree well with the empirical potentials. A similar pattern is found when comparing $U_c(r)$ for the central potentials evaluated at zero energy. Furthermore, the volume integral of the central V_1 term for the RGM potential, ~ 550 MeV fm^3, is very close to the values in Table III, while the rms radius, 2.44 fm, is a little larger than the values in Table III. These results hold in spite of the schematic nature of the N-N interaction. However, for the central V_2 term, the volume integral is about 50% larger in magnitude than the empirical value.

Qualitatively, the RGM and empirical energy dependences agree, since in both cases the central V_1 and V_2 components fall with energy and the V_2 component falls in magnitude some 2 or 3 times faster than the V_1 component. The $\xi_{c\,1}$ agree quantitatively in the linear energy dependent fits. Comparing Tables II and IV, the RGM value of $\xi_{c\,1}$ for the central V_1 term is only slightly less in magnitude than the empirical value and, for the central V_2 term, $\xi_{c\,1}$ falls well within the range of empirical values. The RGM results also predict a small departure from the linear energy dependence whereby $|\xi_{c1}|$ decreases with energy for both central components, as shown in Table I, but second order effects cannot be unambiguously established in inversions from empirical phase shifts. The comparison of the RGM and empirical solutions over the wider energy range is limited by the difficulties in determining potentials accurately at higher energies. The potential shape of the central V_1 part of both the empirical and RGM potentials is fairly constant with energy. However, the central V_2 component obtained from the RGM has significant changes in the radial geometry, as measured in terms of the volume integral and rms radius of $U_c(r)$. In moving from subthreshold energies to energies above the threshold, a decrease is seen in the empirical potentials for both $|J_0|$ and rms radius, but the overall shape dependence is small.

The energy dependence in the single-channel RGM arises from exchange, the N-N interactions being energy independent. The energy dependence is of particular interest since that of the parity independent term of Secs. III A 1 and III A 1 is due to knockon (Fock term) exchange, a process responsible for a large part of the energy dependence of the nucleon-nucleus optical potential. The parity dependent component of the potential arises from different exchange processes, largely ''heavy particle stripping,'' and is expected to fall quite rapidly with energy. The energy dependence of this term for p-α, especially if compared with that for heavier target nuclei, gives a measure of the error involved when processes leading to parity dependence are omitted from calculations of the optical potential.

A full consideration of all channel coupling effects is required to establish rigorously the contributions of antisymmetrization to the imaginary components, and this presents a formidable calculation. However, an estimate of some of the effects on the imaginary components due to the nonlocality implicit in the RGM calculations can be obtained from a much simpler RGM calculation in which the channel coupling is represented by a phenomenological imaginary term [31]. The application of fixed energy inversion to these RGM phase shifts does not yield imaginary potentials which exactly equal the phenomenological potential, because of the nonlocal effects. The central imaginary terms obtained by inversion are close to the input terms [31] in the surface region, but at $r<1$ fm, distinct *generative* features appear which are very similar to the features found for the central V_1 term in Figs. 12 and 14. This supports our view that the generative feature found empirically for the central V_1 imaginary terms is due to nonlocality effects.

VI. CONCLUSIONS

Energy and parity dependent potentials can now be calculated by inversion from S matrices established as a function of energy. The new procedure is restricted only to cases where the potential shape is energy independent. In the most general formulation, the energy dependence in each potential component is expressed as an expansion over an arbitrary basis of energy dependent functions, appropriate to the size of the input data set, but for many practical applications a linear dependence on energy is sufficient. A very accurate inversion is obtained from fitting a linear energy dependence to S-matrix values for a reduced energy range, or ''energy bite,'' from which finer details of the energy dependence or the energy dependence of the potential geometry can be studied. SVD techniques are an essential part of the whole procedure to establish well-behaved potentials using a restricted basis set.

With these new techniques, inversion has been applied to $p+\alpha$ S matrices at energies above the inelastic threshold, representing, in our view, the first time that physical information, in a form suitable for comparison with theoretical models, has been extracted from the experimental data. Complex, energy dependent potentials have been determined which reproduce the empirical S matrices for a wide range of energies up to 70 MeV. Both the real and imaginary components are found to depend on energy and parity, but the imaginary components are small in magnitude and the radial form and the energy dependence are not very well determined. The corresponding real potentials are very similar to the potentials determined at subthreshold energies in both the energy and the parity dependence. A consistent description of the $p+\alpha$ real potential has therefore been established from 0 to $\sim$65 MeV.

The new technique has also been applied to determine energy dependent potentials from RGM phase shifts for $p+\alpha$ and $n+{}^{16}$O scattering. For the RGM phase shifts, as well as for the empirical parametrized phase shifts for $p+\alpha$ at subthreshold energies, the smooth variation with energy permits application of the energy bite techniques. A significant nonlinear energy dependence arises in the central parity dependent component, but for $p+\alpha$, the departures from a linear energy dependence are small and the potential geometry changes slowly with energy.

For $n+{}^{16}$O, the RGM bound state energies can be fitted simultaneously with phase shifts for low energies using a linearly energy dependent potential. A consistent description is thereby obtained for both positive and negative energies. However, no potential could be obtained over a wide energy range for $n+{}^{16}$O, due to a significant energy dependence in the geometry of the small parity dependent term.

Many features in the empirical potential relate directly to the effects of antisymmetrisation. For $p+\alpha$ scattering, the real potentials determined from the RGM phase shifts have all the qualitative features, i.e., the comparative strengths, the geometries, and energy dependences, of the potentials determined from empirical S matrices, at energies both above and below the inelastic threshold. This close agreement, which applies to both the energy dependence of the parity independent and parity dependent central components, represents a significant result of the energy dependent inversion, because of the close relationship of these terms to distinct types of exchange.

There are many empirical phase shift tabulations, above and below the inelastic threshold, which can now be analyzed with energy dependent inversion. The method also allows a far more comprehensive study than has been previously possible of the energy dependence underlying the RGM for a wide variety of cases, some of which are not easily accessible to experiment. Similar applications permit a study of the energy dependence of channel coupling effects, and particularly reaction channel coupling effects, in the nucleon-nucleus interaction so that these effects can be properly understood, at least in the case of light target nuclei.

ACKNOWLEDGMENTS

We are most grateful to the Science and Engineering Research Council of the UK, and its successor EPSRC, for Grant No. GR/H00895 supporting S.G.C.

[1] K. Chadan and P.C. Sabatier, *Inverse Problems in Quantum Scattering Theory*, 2nd ed. (Springer-Verlag, Berlin, 1989).
[2] L.J. Allen, K. Amos, C. Steward, and H. Fiedeldey, Phys. Rev. C **41**, 1001 (1990).
[3] E.K. May, M. Munchöw, and W. Scheid, Phys. Lett. **141B**, 1 (1984).
[4] H. Leeb, W.A. Schnizer, H. Fiedeldey, S.A. Sofianos, and R. Lipperheide, Inverse Problems **5**, 817 (1989).
[5] *Quantum Inversion Theory and Applications*, Proceedings, Bad Honnef, Germany, 1993, edited by H. V. von Geramb (Springer-Verlag, Berlin, 1994).
[6] S.G. Cooper and R.S. Mackintosh, Phys. Rev. C **43**, 1001 (1991).
[7] S.G. Cooper and R.S. Mackintosh, Nucl. Phys. **A517**, 285 (1990).
[8] S.G. Cooper, Phys. Rev. C **50**, 359 (1994).
[9] S.G. Cooper, R.S. Mackintosh, A. Csótó, and R.G. Lovas, Phys. Rev. C **50**, 1308 (1994).
[10] S.G. Cooper and R.S. Mackintosh, Nucl. Phys. **A592**, 338 (1995).
[11] N.W. Schellingerhout, L.P. Kok, S.A. Coon, and R.M. Adam, Phys. Rev. C **48**, 2714 (1993).
[12] Q.K.K. Liu and S.G. Cooper, Phys. Rev. C **51**, 2268 (1995).
[13] G.R. Plattner, A.D. Bacher, and H.E. Conzett, Phys. Rev. C **5**, 1158 (1972).
[14] A. Houdayer, N.E. Davison, S.A. Elbakr, A.M. Sourkes, W.T.H. van Oers, and A.D. Bacher, Phys. Rev. C **18**, 1985 (1978).
[15] S. Burzynski, J. Campbell, M. Hammans, R. Henneck, W. Lorenzon, M.A. Pickar, and I. Sick, Phys. Rev. C **39**, 56 (1989).
[16] T. Saito, Nucl. Phys. **A331**, 477 (1979).

[17] D. Baye, J. Phys. A **20**, 5529 (1987).
[18] I. Reichstein and Y.C. Tang, Nucl. Phys. **A158**, 529 (1970).
[19] T. Kaneko, M. LeMere, and Y.C. Tang, Phys. Rev. C **45**, 2409 (1992).
[20] G.R. Satchler, L,W. Owen, A.J. Elwyn, G.L. Morgan, and R.L. Walter, Nucl. Phys. **A112**, 1 (1968).
[21] S.G. Cooper and R.S. Mackintosh, Open Univerity Report No. OUPD9602, 1996.
[22] R.S. Mackintosh and A.M. Kobos, Phys. Lett. **116B**, 95 (1982); A.A. Ioannides and R.S. Mackintosh, Nucl. Phys. **A438**, 354 (1985).
[23] A.A. Ioannides and R.S. Mackintosh, Nucl. Phys. **A467**, 482 (1987).
[24] S.G. Cooper and R.S. Mackintosh, Inverse Problems **5**, 707 (1989).
[25] S.G. Cooper and R.S. Mackintosh, Users manual for IMAGO, Open University Report No. OUPD9201, 1992.
[26] Th. Stammbach and L.R. Walter, Nucl. Phys. **A180**, 225 (1972).
[27] P. Schwandt, T.B. Clegg, and W. Haeberli, Nucl. Phys. **A163**, 432 (1971).
[28] S.G. Cooper and R.S. Mackintosh, presented at the Conference on ''Clusters in Nuclear Structure and Dynamics,'' Strasbourg, 1994 (unpublished).
[29] R.A. Arndt, L.D. Roper, and R.L. Shotwell, Phys. Rev. C **3**, 2100 (1971).
[30] R.L. Varner, W.J. Thompson, T.L. McAbee, E.J. Ludwig, and T.B. Clegg, Phys. Rep. **201**, 57 (1991).
[31] D.R. Thomson, Y.C. Tang, and Ronald E. Brown, Phys. Rev. C **5**, 1939 (1972).